Online Research @ Cardiff

information services
gwasanaethau gwybodaeth

Design and validation of a battery management system for solar-assisted electric vehicles

Hongqian Wei [a,b,c], Yan Zhong [a,b], Likang Fan [a,b], Qiang Ai [a,b], Wenqiang Zhao [a,b], Rui Jing [c*✉],

Youtong Zhang [a,b*✉]

a School of Mechanical Engineering, Beijing Institute of Technology, Beijing 100081, China

b Key Lab of Beijing Low Emission Vehicle, Beijing 100081, China

c School of Engineering, Cardiff University, Cardiff CF24 3AA, UK

Abstract: Expanding the travel mileage of power batteries is of great significance for electric vehicles (EVs). The solar battery pack is considered as a promising supplement to the battery management system (BMS) of EVs but integrating solar power into EVs remains a challenge. This paper proposes a BMS that coordinates the solar panels and the lithium battery system. The proposed BMS mainly involves three aspects. Firstly, an equivalent second-order resistance-capacitance model is established and afterwards is identified by using an improved recursive least squares algorithm. Then, the maximum power prediction strategy is developed based on the advanced state of charge (SOC) algorithm and the available solar energy estimation algorithm. Thirdly, a multi-stage constant current charging strategy based on the adaptive genetic algorithm is designed to optimize the battery temperature rise and charging time simultaneously. The proposed BMS is validated by the experiment on a real-world solar-assisted EV. The results indicate that the proposed power prediction strategy can accurately estimate the available power for EVs. Compared with the widely-used charging method, the developed optimal

charging strategy reduces the charging time and temperature rise by 7%-11% and 36%-45%, respectively.

Keyword: electric vehicles; battery management system; photovoltaic cell; solar energy; energy schedule; model and optimization

_____

∗ Corresponding author: Youtong Zhang; Rui Jing

✉ Email address: youtong@bit.edu.cn(Y. Z.); fafujingrui@126.com(R. J.)

Abbreviation			
EV	electric vehicle	MPPT	maximum power point tracking
BMS	battery management system	RLS	recursive least squares
SOC	state of charge	PSO	particle swarm optimization
SOP	state of power	RC	resistance capacitance
SOH	state of health	AH	ampere hour integration
EKF	extended Kalman filter	OCV	0pen circuit voltage
UKF	unscented Kalman filter	UCV	ultimate current value
PSO	particle swarm optimization	RC	resistance and capacitor
GA	genetic algorithm	CCCV	constant current constant voltage
PC	pulse current	MCC	multi-stage constant current

1 Introduction

Climate change has promoted the decarbonization of transport sector via electrification globally. EVs are one promising and cost-effective solution due to their high energy conversion efficiency and low pollutant emissions [1]. Nevertheless, challenges remain for the battery systems, such as short endurance mileage, high replacement cost and high maintenance cost. Cooperating EV power with other clean energy is expected as an alternative to address those challenges [2], among which the sustainable solar energy plays a key role by deploying it as an auxiliary power source for EVs. The electricity generated by the photovoltaic system can either be directly utilized to power electric machines for releasing the burden of the original BMS [3] or been charged into the battery for later use so as to extend the EVs driving mileage [4, 5]. Therefore, the solar-assisted EVs could be an important solution for decarbonizing the transport sector.

1.1 Literature review

The power battery pack and its management technology affect the overall performance of EVs. Significant research efforts have been spent on the BMS aiming for the accurate battery modelling and state estimation [6], peak power optimization [7], charging optimization and life safety assessment [8].

The SOC value characterises the available battery electricity, which determines the degree of safe driving and provides an important reference to other battery states, such as state of health (SOH) and state of power (SOP). The ampere-hour (AH) integration method based on

3

characteristic parameters was first adopted to estimate the battery SOC [9]. However, the accumulated error caused by the current integration function seriously affects the estimation accuracy. Therefore, the model-based SOC estimation methods have received increasing attention. In the past decades, Kalman filter method [10, 11], slide mode observer [12], H∞ filter and particle filter [13] have been widely utilized. G. L. Plett [14] adopted the first-order Taylor expansion to linearize the nonlinear battery model in the extended Kalman filter (EKF), however, the estimation accuracy of this method could be limited due to the segmented approximation. Thus, the unscented Kalman filter (UKF) was then employed to address the nonlinear error existing in the traditional EKF method [15]. To further address the uncertain status error and unknown noise in the UKF method, Peng *et al*. [16] introduced a forgetting factor to estimate the noise and performed the memory fading process. In [17], the EKF and adaptive UKF methods are further combined to estimate SOC and SOH values. However, the increasing estimation accuracy incurs the heavy computational burden which is challenging for the practical BMS. Therefore, the trade-off between accurate estimation of SOC in the low-battery mode and its executability is a pain point in existing studies.

The SOP value characterises the maximum charging and discharging power of a battery pack under the premise of safety, which is directly related to the acceleration and climbing performance of EVs. Two categories of SOP prediction methods are available, i.e., the experimental look-up table method and the model predictive method. The former method captures the peak charging/discharging power at a fixed SOC point by calculating the open circuit voltage and internal resistance under the hybrid pulse excitation [18]. However, this

method does not consider the polarisation current, resulting in the low prediction accuracy. The latter method obtains the ultimate currents with estimated SOC values, which constrains the cut-off voltage for the charging/discharging processes. In [19], the aging of power battery pack is considered and the initial state error is well corrected with the joint estimation of SOC and SOP values. In [20], the Butler-Volmer equation model is proposed to constrain the voltage drop, which can acquire the predicted SOP value within 10s through a fixed current excitation. However, the heavy computational burden makes it hard to execute in practical vehicles. Xiong *et al.* [21] utilized the genetic algorithm to identify battery parameters and proposed a multi-parameter constraint SOP method, which considered the internal resistance and hysteresis characteristics. The experimental results indicate the method is more accurate and reliable than the singe parameter restriction method.

Another important task of BMS is to optimize the charging process, which aims to improve the charging efficiency in the premise of charging safety. Currently, the widely used charging strategy includes the constant current constant voltage (CCCV) charging strategy [22], pulse current (PC) charging strategy [23], and multi-stage constant current (MCC) charging strategy [24]. The CCCV charging strategy is to charge the battery with the constant current and voltage mode, which has the clear logic and simple operation [22]. On this basis, the intermittent charging mode was developed to decrease the temperature rise of batteries [25]. The PC charging strategy would generate the positive pulse currents to charge the battery and generate the negative currents to discharge for depolarisation and higher charging peak currents. In this way, the total charging time was reduced by about 20% than the CCCV charging strategy [26]. In [23], the frequency-

5

varied and duty-varied pulse charging mode was optimized considering the minimal impedance. A significant finding was that the charging time was reduced only within the 0-0.2 SOC intervals, however, the battery polarisation value was hard to measure in real vehicles. The MCC method is to optimize the charging current according to different SOC values [24]. For instance, the particle swarm optimization (PSO) algorithm can optimize the charging ratio and charging time, in which the charging time was reduced by 57% but the charging efficiency was reduced by 0.5% than the CCCV method [27]. Similarly, the multiple-PSO method can optimize the charging time and charging loss, in which the optimal charging current in each SOC interval is calculated [28]. In general, with consideration of the charging characteristics, the charging order and charging current curve can be optimized to improve the charging performance of the battery pack. However, fewer studies have modelled the temperature rise in the charging process; uncontrollable temperature rise would cause the thermal runaway and possible safety accident.

1.2 Knowledge gap and contributions

Seen from the literature review, research towards the battery pack of EVs should focus more on the driving mileage and cleaning applications. The solar panels could generate the electricity to power the electric machines or charge the battery to extend the EVs driving mileage. Besides, the solar panels generate zero pollutant emission, which is environmentally friendly to the future green travel. Accordingly, integrating the solar panels in the EVs provide a promising solution for the decarbonization of transport sector. However, existing research focuses on the battery applications, such as battery state estimation, battery charging optimization or battery life evaluation, little research has been executed to explore the potential of integrating the lithium

battery with the green solar energy. To fill this knowledge gap, this study for the first time models a solar-assisted battery system which is underpinned by considering the battery state estimation and optimal charging strategy.

Specifically, a second-order equivalent battery model is established, and characteristic parameters, including the resistance, capacitance and open circuit voltage, are identified by using the improved recursive least squares (RLS) algorithm. The joint EKF-AH algorithm is then applied to accurately estimate SOC values in whole intervals. On this basis, the maximum power point tracking (MPPT) algorithm is designed to model the solar generation which is utilized to predict the SOP value. The optimization of charging process is another importance issue of the proposed BMS. Considering the lessening of charging time benefits to the labour cost and work efficiency, the primary optimization objective adopts the charging time. Besides, the optimization of charging current also should consider the battery temperature in the charging process for the guarantee of battery health and charging performance. Accordingly, the multi-stage constant current charging approach is designed to optimize the temperature rise and charging time simultaneously. More importantly, the proposed BMS is embedded into a real-world solar-assisted EV experimental platform. The advantages of the modelled integrated battery system, joint maximum power prediction strategy, and the optimal charging strategy are validated.

Conclusively, this study **contributes** to the following points:

(1) This study for the first time explores the potential of integrating solar energy into EVs by both mathematical modelling and experimental validation. Synergistic energy management of

solar energy system and lithium-ion battery system turns out to benefit the electricity utilization in EVs, which implies a multi-sector integrated solution to extend travel mileage and contribute to deep decarbonization of transport sector.

(2) The synergetic strategy of SOC estimation and SOP prediction strategies were designed based on the improved second-order RLS parameter estimation algorithm. The electricity generated by the solar panels is estimated and the real-time SOC both take effect to estimate the maximum power of EVs.

(3) An efficient charging strategy towards the multiple objectives of temperature rise and charging time was deployed. An adaptive-weighted factor has been applied to coordinate both objectives and the online genetic algorithm (GA) is utilized to solve the optimal charging currents in real time. The hardware experiment has been implemented to validate its executability in a real-world solar-assisted EV.

2 Proposed BMS and parameter identification

2.1 Framework of the proposed BMS

This section describes the framework of the proposed EMS as shown in **Fig. 1**. Firstly, the offline experiment is implemented to explore the battery characteristics, which are expressed in **Appendix A.1**. Accordingly, a second-order equivalent resistance and capacitance (RC) battery circuits and solar panel circuit are modelled, and afterwards temperature rise model is established. On this basis, the improved RLS algorithm is developed to identify the battery parameters, such as the battery resistance, capacitance and open-circuit voltage. With the

battery model, the maximum available power of the solar-assisted EV is predicted in **Section 3** and the efficient charging strategy is thereby optimized in **Section 4**. Concretely, a novel EKF-AH algorithm is proposed to estimate the battery SOC, which is utilized to limit the SOP value of EVs and the available solar power is also coordinated to correct the final SOP values. Finally, the optimal charging strategy is proposed which aims at optimizing the temperature rise and charging time, simultaneously. To accelerate the solving process of the optimization, the adaptive GA approach is developed.
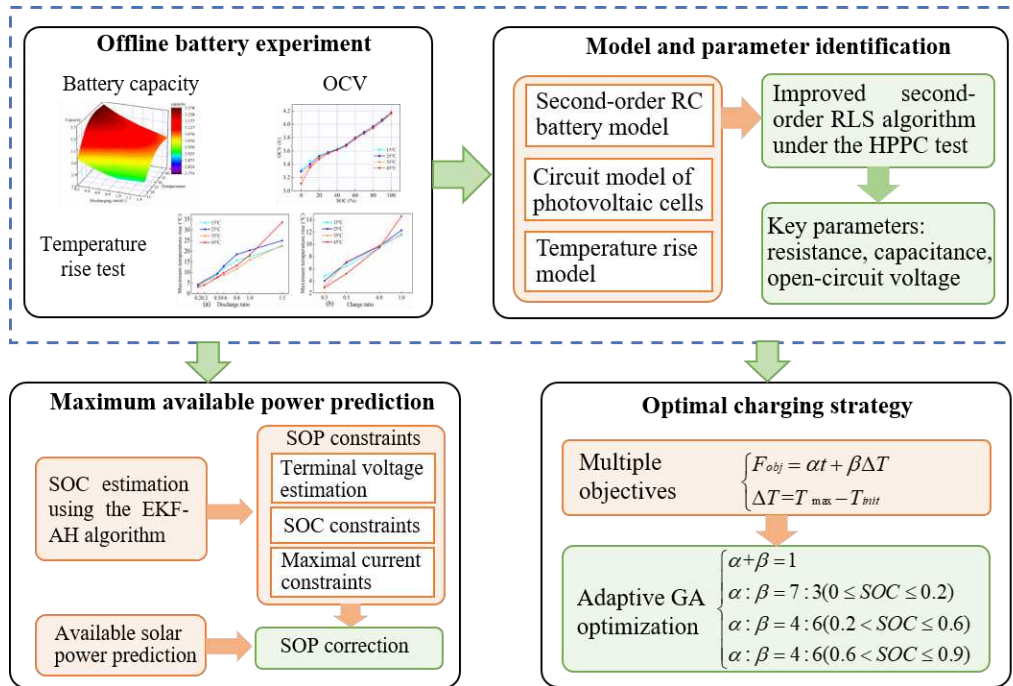
Fig. 1 Framework of the proposed BMS.

Fig. 2 illustrates the battery models and the solar panel characteristics. To improve the model accuracy, a second RC circuit is developed as shown in **Fig. 2(a)** and the single diode circuit model for solar panels are exhibits in **Fig. 2(b).** The layout of roof mounted solar panels is shown in **Fig. 2(c).** Then, the electric characteristics of solar panels under different radiation and intensities and temperatures are displayed in **Fig. 2(d)** and **(e)**, respectively. The details

9

associated with the sub-figures will be explained in the following sub-sections.
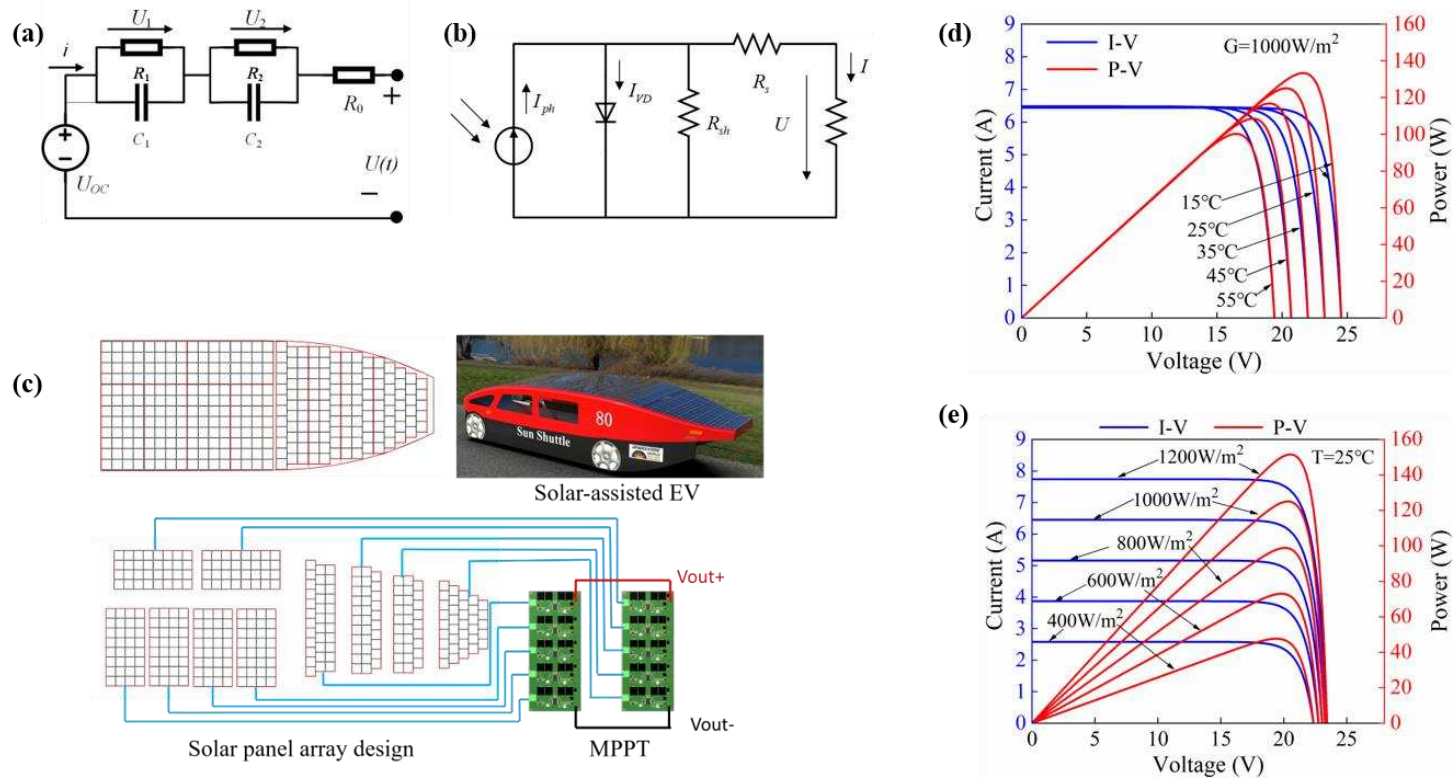
Fig. 2 Battery models and experimental results of solar panels. (a) Second-order RC battery equivalent circuit model; **(b)** Single diode

circuit model of solar panels; **(c)** Roof mounted solar panel array design for the solar-assisted EV; **(d)** Solar panel characteristics under different

radiation intensities; **(e)** Solar panel characteristics under different temperatures.

2.2 System model construction

2.2.1 Battery equivalent circuit model

The equivalent battery circuit model adopts the voltage source to represent the thermodynamic equilibrium potential. In this study, we adopt the second-order RC model to construct the equivalent battery circuit as shown in **Fig. 2(a),** which has two RC circuits in parallel and exhibits bipolar characteristics to represent the charge transfer and diffusion process [29], where U_{oc} and R_o represent the open-circuit voltage and internal resistance. $R_1 C_1$ and $R_2 C_2$ are adopted to simulate the polarisation reaction, in which U_1, R_1, C_1 denote the polarisation voltage, resistance and capacitance of cell electrochemistry, respectively, while U_2, R_2, C_2 denote the concentration polarisation voltage, resistance and capacitance, respectively.

According to the equivalent principle, the equivalent formulation can be formed in Eq. (1).

$$
\begin{cases}
Uoc = iR_0 + U_1 + U_2 + U(t) \\
i = \dfrac{U_1}{R_1} + C_1 \dfrac{dU_1}{dt} \\
i = \dfrac{U_2}{R_2} + C_2 \dfrac{dU_2}{dt}
\end{cases}
\tag{1}
$$

The output of RC circuits consists of two parts: one is the zero-state response produced by the external current excitation; another is the zero-input response determined by the initial state without the external excitation. The specific zero-state response is depicted in Eq. (2).

$$
\begin{cases}
U_{1,k+1}^{zs} = I_k R_1 \times \left(1 - e^{(-\Delta t/\tau_1)}\right) \\
U_{2,k+1}^{zs} = I_k R_2 \times \left(1 - e^{(-\Delta t/\tau_2)}\right)
\end{cases}
\tag{2a}
$$

12

$$\begin{cases} \tau_1 = R_1 \times C_1 \\ \tau_2 = R_2 \times C_2 \end{cases} \tag{2b}$$

where $U_{1,k+1}^{zs}$ and $U_{2,k+1}^{zs}$ denote the zero-state response voltages in both RC circuits; Δt is the control period; τ_1 and τ_2 are time constants. The zero-input response is formulated in Eq. (3).

$$\begin{cases} U_{1,k+1}^{zp} = \mathrm{e}^{(-\Delta t/\tau_1)} \times U_{1,k} \\ U_{2,k+1}^{zp} = \mathrm{e}^{(-\Delta t/\tau_2)} \times U_{2,k} \end{cases} \tag{3}$$

Therefore, the voltage response on the output terminals is the sum of zero-state response and zero-input response, see Eq. (4).

$$\begin{cases} U_{1,k+1} = U_{1,k+1}^{zp} + U_{1,k+1}^{zs} = \mathrm{e}^{(-\Delta t/\tau_1)} \times U_{1,k} + I_k R_1 \times \left(1 - \mathrm{e}^{(-\Delta t/\tau_1)}\right) \\ U_{2,k+1} = U_{2,k+1}^{zp} + U_{2,k+1}^{zs} = \mathrm{e}^{(-\Delta t/\tau_2)} \times U_{2,k} + I_k R_2 \times \left(1 - \mathrm{e}^{(-\Delta t/\tau_2)}\right) \end{cases} \tag{4}$$

2.2.2 Solar panel model

The solar panels adopt the Me3-Si photovoltaic (PV) cell which is composed of semiconductor diodes. A solar circuit model is established based on the electronic characteristics [30], as shown in **Fig. 2(b).** Parameters of the Si PV cell are listed in **Table 1**.

Table 1 Parameters of single Si PV cell.

Parameters	Values
Packing factor	82.9%
Efficiency	25%
Size	125mm*125mm
Short-circuit current	6.45A
Open-circuit voltage	0.727V

Maximum power	3.89W
Voltage at the maximum power point	0.64V
Current at the maximum power point	6.08A

According to the Kirchhoff's theorem, the output current of solar panels is depicted in Eq. (5a).

$$I = I_{ph} - I_{VD} - I_{sh} \quad (5a)$$

$$s.t. \quad \begin{cases} I_{VD} = I_0 \left[\exp\left(\frac{q(U + IR_s)}{AkT} \right) - 1 \right] \\ I_{sh} = \frac{U + IR_s}{R_{sh}} \end{cases} \quad (5b)$$

where I_0 denotes the reverse saturation current of a solar cell under the condition of zero radiation; $q=1.6\times10^{-19}$C denotes the unit charge; $A=1.2$ is the correction factor; $k=1.38\times10^{-23}$J/K is the Boltzmann constant; T denotes the surface temperature of the PV cell. Substituting the Eq. 5(b) into Eq. 5(a), the output current can be obtained as shown in Eq. (6).

$$I = I_{ph} - I_0 \left[\exp\left(\frac{q(U + IR_s)}{AkT} \right) - 1 \right] - \frac{U + IR_s}{R_{sh}} \quad (6)$$

The photogenerated current I_{ph} and reverse saturation current I_0 can be solved with Eq. (7).

$$\begin{cases} I_{ph} = \frac{0.001 \square (T - T_r) + I_{sc}}{G_{ro}} \square G_r \\ I_0 = I_{rs} \left(\frac{T}{T_r} \right)^3 \exp\left[\frac{qE_g}{Bk} \left(\frac{1}{T_r} - \frac{1}{T} \right) \right] \end{cases} \quad (7)$$

where $T_r = 298.15K$ denotes the reference operative temperature; I_{sc} denotes the short-circuit current; G_r is the actual radiation intensity and $G_{r0} = 1000W/m^2$ is the ideal radiation intensity; I_{rs} is the saturation current; $E_g = 1.1$ denotes the forbidden width length of semiconductor materials. $B=1.2$ is the scaling factor.

For the practical solar-assisted EV, if a solar panel array is composed of N_s solar panels in series and N_p panels in parallel, the actual equivalent current can be calculated by Eq. (8).

$$I = I_{ph} - I_d - I_p \tag{8a}$$

$$\text{Series current} \qquad I_p = \frac{U N_p / N_s + I R_s}{R_{sh}} \tag{8b}$$

$$\text{Parallel current} \quad I_d = \left(\exp\left[\frac{q(U / N_s + I R_s / N_p)}{AkT} \right] - 1 \right) I_0 N_p \tag{8c}$$

In this study, the actual vehicle has 10 sets of solar panel arrays, and each set is composed of 32 solar cells connected in series. The roof structure and array design of the solar-assisted EV are shown in **Fig. 2(c)**.

The characteristic curves of solar panels under different radiation intensities and temperatures are shown in **Fig. 2(d)** and **Fig. 2(e)**, respectively. In **Fig. 2(d)**, with the increase of radiation intensity, the short-circuit current and maximum power of solar panel arrays increase rapidly, which manifests that the maximum power of 1200W/m² radiation intensity is twice that of 400W/m². Meanwhile, with the radiation intensity increases, the voltage at the maximum power point increases slightly. In **Fig. 2(e)**, as the temperature increases, the short-circuit maintains almost stable, but the voltage at the maximum power point decreases and the maximum power is also reduced accordingly. According the experimental test, when the temperature of the solar panel array decreases by 10℃, its power increases by 8W, accounting for 6%-8%.

Based on the above analysis, the power generation of solar panels is greatly affected by the radiation intensity, but less affected by the temperature (only when the temperature difference is larger than 10℃, the power generation is affected, such a situation is rare in practice).

15

Therefore, the short-term power generation prediction needs to consider the influence of radiation intensity on the solar power prediction algorithm while the impact of the temperature could be neglected.

2.2.3 Battery temperature rise model

Since the heat dissipation requirement is significant in the dynamic charging process, the temperature rise is modelled. When the charging current is within a reasonable range, the lithium battery can be regarded as a mass point with a uniform surface temperature. Therefore, its heat model can be expressed by Eq. (9).

$$mC_{\text{cell}}\frac{dT_{\text{cell}}}{dt} = Q_{\text{S}} + Q_0 - Q_{\text{B}} \tag{9}$$

where m denotes the mass of a single cell; Q_S, Q_0, and Q_B are the heat of reversible reaction with the entropy difference ΔS, the heat loss, and the transferred heat, respectively. T_{cell} and C_{cell} are the battery temperature and heat capacity. The Q_S, Q_0, and Q_B can be further formulated with the temperature difference between the battery surface and environment as shown in Eq. (10).

$$\begin{cases} Q_{\text{S}} = T_{\text{cell}}\Delta S\,\dfrac{I}{nF} \\ \Delta S = -\dfrac{\partial \Delta G}{\partial T_{\text{cell}}} = nF\,\dfrac{\partial E}{\partial T_{\text{cell}}} \end{cases} \tag{10a}$$

$$Q_{\text{B}} = hA\left(T_{\text{cell}} - T_{\text{amb}}\right) \tag{10b}$$

$$Q_0 = I(U_{oc} - U_t) \tag{10c}$$

where T_{amb} denotes the environmental temperature; A is the surface area of batteries; and h represents the heat transfer coefficient. Substituting Eq. (10) with Eq. (9), the battery

temperature can be formulated by Eq. (11).

$$T_{\text{cell},k} = T_{\text{cell},k-1} + \frac{I^2 R_0 + I U_{1,\text{P}} + I U_{2,\text{P}} + T_{\text{cell},k-1} I \dfrac{\partial E}{\partial T_{\text{cell}}} - Ah\left(T_{\text{cell},k-1} - T_{\text{amb}}\right)}{mC_{\text{cell}}}$$

(11)

2.3 Parameter identification

This section develops an offline improved RLS algorithm to identify battery parameters in the second-order RC model. The details can be found in **Fig. 3**. In this study, hybrid pulse power characteristic (HPPC) condition is applied to test batteries as depicted in **Fig. 3(a)**. Explicitly, stage *a-b* denotes the constant current charging condition which enables the battery to operate in different SOC intervals. Stage *b-i* denotes that the battery is statically placed for 1 h, during which the second-order time constant τ_2. is identified. Stage *i-j* denotes the multi-ratio discharging conditions, in which the improved RLS algorithm [31] is utilized to identify the internal resistance R_0 and first-order RC time constants τ_1.
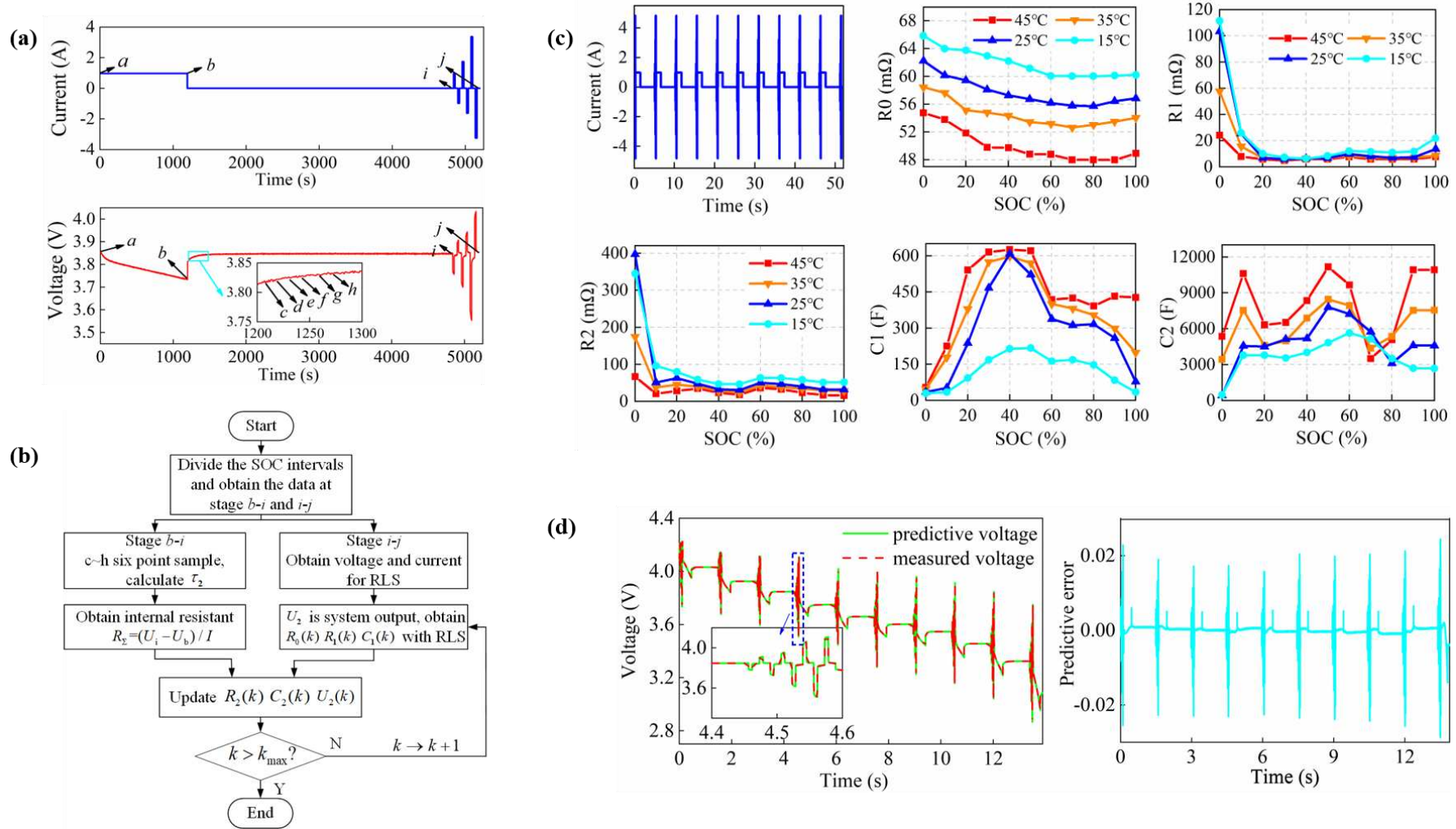
Fig. 3 Parameter identification. (a) HPPC condition; **(b)** Flowchart of the improved offline RLS algorithm; **(c)** Identified parameters of lithium batteries under different temperatures; **(d)** Identification result validation under the HPPC condition at 45 ℃.

18

In the stage of *b-i*, the slightly increasing voltage is closely related with the time constant τ_2.

Thus, according to Eq. (3), the voltage rise can be formulated as Eq. (12).

$$U_t = U_{oc} - U_1 e^{-t/\tau_1} - U_2 e^{-t/\tau_2} \tag{12a}$$

$$U_2 e^{-t/\tau_2} = U_i - U_t \tag{12b}$$

where U_i denotes the terminal voltage at point *i*; U_t represents the initial terminal voltage and

U_2 denotes the polarisation voltage with time constant τ_2. By selecting two points in the stage

b-i, the time constant τ_2 can be solved by Eq. (13).

$$\tau_2 = \frac{t_d - t_c}{\ln(U_i - U_c) - \ln(U_i - U_d)} \tag{13}$$

Besides, in the constant current discharging stage *a-b*, the charge time is up to 20min, which

means that the polarisation capacitance C_1 and C_2 are relatively stable. Thus, at the point *b*,

the following equation is depicted as Eq. (14).

$$U_i - U_b = I(R_0 + R_1 + R_2) = IR_\Sigma \tag{14}$$

With the above formulations, the sum of three internal resistances R_Σ can be solved.

Therefore, according to the above derivations, parameters including τ_2 and R_Σ, are obtained.

The following parameters of R_0, R_1 and C_1 can be identifies with offline RLS algorithm. With

τ_2 and R_Σ, the polarisation voltage U_2 can be utilized to represent system outputs derived by

Eq. (15).

$$\begin{cases} U_b(s) = U_{oc}(s) - U_2(s) - U(s) \\ U_2(s) = \dfrac{R_2}{\tau_2 s + 1} I(s) \\ U_b(s) = R_0 I(s) + \dfrac{R_1}{\tau_1 s + 1} I(s) \end{cases} \tag{15}$$

19

where $U_b = U_2$ and the SOC at the stage of *i-j* is regarded constant, therefore, $U_{oc} = U_i$. By discretizing Eq. (15), the differential equation is formulated as Eq. (16).

$$\begin{cases} U_b(k) = U_i - U_2(k) - U(k) \\ U_b(k) = U_b(k-1)\dfrac{\tau_1}{T+\tau_1} + I(k)\dfrac{T(R_0+R_1)+R_0\tau_1}{T+\tau_1} - I(k-1)\dfrac{R_0\tau_1}{T+\tau_1} \end{cases} \tag{16a}$$

$$\begin{cases} a_1 = \dfrac{\tau_1}{T+\tau_1} \\ a_2 = \dfrac{T(R_0+R_1)+R_0\tau_1}{T+\tau_1} \\ a_3 = -\dfrac{R_0\tau_1}{T+\tau_1} \end{cases} \tag{16b}$$

where parameters a_1, a_2, and a_3 are the coefficients, constituting the parametric matrix. The system matrix in the RLS is defined in Eq. (17).

$$\begin{cases} \phi(k) = \left[U_b(k-1) \quad I(k) \quad I(k-1)\right]^{\mathrm{T}} \\ \theta(k) = \left[a_1(k) \quad a_2(k) \quad a_3(k)\right]^{\mathrm{T}} \\ U_b(k) = \phi^{\mathrm{T}}(k)\theta(k) \end{cases} \tag{17}$$

The execution of RLS algorithm is thereby described as following four major steps and the flowchart can be found in **Fig. 3(b).**

Step (1): The system matrix is defined and initialized. The system matrix including gain matrix, parametric update matrix and covariance matrix $\theta(0) = 0.001 * ones(5,1)$, $P(0) = 10^6 I_{5\times5}$ and $U_2(0) = 0$, should be initialized. The main recursive process is defined in Eq. (18).

$$y_k = \phi(k)\theta(k) \tag{18a}$$

Gain matrix $\quad K(k) = P(k-1)\phi(k)\left[\phi^{\mathrm{T}}(k)P(k-1)\phi(k)+\lambda\right]^{-1} \tag{18b}$

Parametric update $\quad \hat{\theta}(k) = \hat{\theta}(k-1) + K(k)\left[y(k)-\phi^{\mathrm{T}}(k)\hat{\theta}(k-1)\right] \tag{18c}$

Covariance matrix $\quad P(k) = \dfrac{1}{\lambda}\left[I - K(k)\phi^{\mathrm{T}}(k-1)\right]P(k-1) \tag{18d}$

20

Step (2): Battery model parameters of R_0, R_1 and C_1 can be solved by Eq. (19).

$$\begin{cases} \tau_1(k) = \dfrac{a_1(k)T}{1-a_1(k)} \\[2mm] R_0(k) = -\dfrac{a_3(k)\big(\tau_1(k)+T\big)}{\tau_1(k)} \\[2mm] R_1(k) = \dfrac{a_2(k)\big[\tau_1(k)+T\big]-R_0(k)\tau_1(k)}{T-R_0(k)} \\[2mm] C_1(k) = \dfrac{\tau_1(k)}{R_1(k)} \end{cases} \tag{19}$$

Step (3): Second-order model parameters of R_2 and C_2 are solved by Eq. (20).

$$\begin{cases} R_2(k) = R_\Sigma - R_0(k) - R_1(k) \\[2mm] C_2(k) = \dfrac{\tau_2(k)}{R_2(k)} \end{cases} \tag{20}$$

Step (4): The polarisation voltage $U_2(k)$ in the τ_2 stage is updated.

$$U_2(k+1) = U_2(k)\left(1-\frac{T}{\tau_2}\right)+I(k)\frac{R_2(k)T}{\tau_2} \tag{21}$$

In the experimental test, the excitation current and identified parameters under four temperature conditions (15℃, 25℃, 35℃ and 45℃) are shown in **Fig. 3(c)**. The electrical parameters vary significantly in the different temperatures and different SOC intervals.

Besides, the HPPC test condition is applied to validate the effectiveness of the identified model parameters. The actual battery terminal voltage and the predictive terminal voltage with the estimated parameters are illustrated in **Fig. 3(d)**. The predictive voltage can always follow the actual voltage change with a little deviation. Even though this error slightly increases under the lower SOC conditions, the actual error still behaves lower than 20mV, which implies the designed offline RLS method is effective for the whole parameter identification.

3 Maximum power prediction strategy for EVs

The maximum power of a solar-assisted EV benefits to explore its ultimate driving ability under accelerating and climbing conditions. This section develops the maximum available power prediction strategy. Specifically, the battery SOC is preliminarily estimated by the advanced EKF-AH algorithm, which is formulated as one important part of the SOP derivation. Afterwards, the available solar energy is obtained based on the predictive maximum power point tracking (MPPT) algorithm. Accordingly, the maximum power prediction strategy, also named SOP prediction strategy, is significantly introduced.

3.1 SOC estimation using the EKF-AH algorithm

Since the SOP is constrained by the battery SOC, a highly accurate SOC estimation algorithm, named EKF-AH algorithm, is developed. The SOC estimation approach is developed in which the improved EKF approach toward second-order RC model is utilized to enhance the estimation accuracy and the ampere hour integration approach is utilized to address the model distortion problem in the lower SOC intervals. To simply this article, more details about the SOC estimation algorithm is described in **Appendix A.2**.

3.2 Available solar power prediction

According to the power output characteristics of solar panels, the inflection point of the P-V curves denotes the maximum power point. The MPPT algorithm is designed to adjust the conduction frequency of power devices to modulate the output voltage of solar panels guaranteeing the maximum power output. In this study, we adopt the adaptive fixed voltage

optimization to track the maximum power point. The primary principle is to preliminarily determine the maximum power point, and then sample the power conditions at three points. Through simulating the characteristic curves, the maximum power point position can be solved. Through the hysteresis comparison method, the above maximum power point can be modified by comparing the real-time power and the estimated power. Finally, the real-time maximum power point of the solar panel array can be obtained cyclically. The details are expressed as below.

(1) Before connecting the loads to solar panels, open circuit voltage is measured, and the preliminary estimation of the maximum power point is calculated by $V_{set1} = k \times V_{oc}$. The MPPT devices regulate the power switches to set the output voltage V_{set1} and then sample the output current, so that the output power of the first point can be calculated accordingly.

(2) The second and third points are determined by adding small disturbance variables. Two disturbance variables $V_{set1} - \Delta V$ and $V_{set1} + \Delta V$ on the left and right sides of V_{set1} are determined, and then the MPPT devices would track these two voltages and calculate their output powers as the second and third points.

(3) The maximum power point is stimulated with the Newton interpolation method in Eq. (22).

$$N(x) = f(x_0) + f(x_0, x_1)(x - x_0) + f(x_0, x_1, x_2)(x - x_0)(x - x_1) \qquad (22a)$$

$$\begin{cases} f(x_0) = y_0 \\ f(x_0, x_1) = \dfrac{f(x_0) - f(x_1)}{x_0 - x_1}, f(x_1, x_2) = \dfrac{f(x_1) - f(x_2)}{x_1 - x_2} \\ f(x_0, x_2) = \dfrac{f(x_0, x_1) - f(x_1, x_2)}{x_0 - x_2} \end{cases} \qquad (22b)$$

Based on the P-V curve in **Fig. 2**. Three sample points are calculated with Eq. (22a) for the stimulated curves. Thus, the stimulated maximum power point is obtained by $dN(x)/dx = 0$.
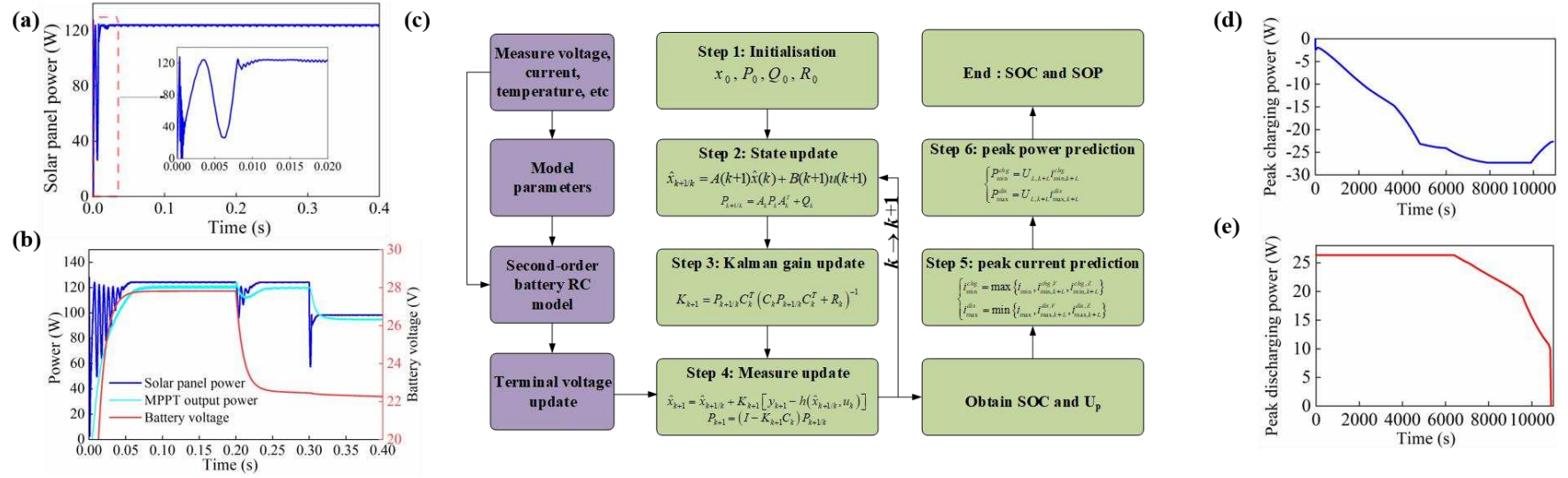
Fig. 4 Predictive solar power results and the SOP prediction algorithm. (a) Original solar power results; **(b)** Solar power results with variant voltage

and radiation intensity; **(c)** Joint SOC/SOP prediction algorithm; **(d)** SOP results in the discharging process; **(e)** SOP results in the charging process.

$$V_{\max} = \frac{\left(x_0 + x_1 - \dfrac{y_1 - y_0}{x_1 - x_0}\right)(x_2 - x_0)}{2\left(\dfrac{y_2 - y_1}{x_2 - x_1} - \dfrac{y_1 - y_0}{x_1 - x_0}\right)} \tag{23}$$

(4) The MPPT device regulates the operative voltage to the calculated maximum voltage point, i.e. $V_{set} = V_{max}$, and the maximum power P_{max} can be determined accordingly.

The original generation power using the above approach without being connected into the lithium battery is illustrated in **Fig. 4(a)**, in which the MPPT can quickly track the maximum power and stabilise at 124W. To explore the effect of the dramatical voltage change and solar radiation variation on the MPPT strategy, a group of variable loads and stepped solar radiation intensity command are applied at 0.2s and 0.3s, respectively as depicted in **Fig. 4(b)**. Compared with the original power curve in **Fig. 4(a)**, the connection of battery pack significantly impacts the fluctuation of tracking power at the start stage of t=0.05s. When the loads at t=0.2s are applied, the battery voltage decreases dramatically from 27.5V to 22.5V. Although the MPPT can again optimize to maintain at the maximum power point of solar panels as much as possible, the output power of MPPT device has been reduced from 121.06W to 117.64W, which implies that the MPPT boosting efficiency has been pulled down. The experimental results show that the booster efficiency of MPPT device is reduced from 97.24% to 94.10% due to the dramatical change in the terminal voltage. When the solar radiation intensity is reduced by 200 W/m², the output power of MPPT is decreased to 95W and the booster efficiency is only 91.57%.

The above analysis implies that the fixed voltage optimization method can track the maximum power point. However, the booster efficiency of MPPT would be pulled down, which would impact the accurate prediction of SOP state of batteries. To accurately predict the effective output

power of MPPT, the following modification is adopted in this study. Since the duration of the peak power is relatively short, the temperature change can be regarded as a constant in a single control period and only the radiation intensity is considered. The final predictive power selects the minimum predictive power within a continuous duration. Therefore, the power prediction correction for L sampling periods at current time k can be processed according to Eq. (24).

$$P_{\max,k+L}^{l} = \min\left(\sum_{i=1}^{L} E_{k.k+L}^{i} \eta S \right) \tag{24}$$

where $E_{k.k+L}^{i}$ denotes the radiation intensity at timeslot i, and η denotes the generation efficiency of solar panels, and S is the effective area of the solar panel.

Another important issue is to address the dramatical voltage drop. When the battery voltage is pulled down to the cut-off voltage, the generated voltage of solar panel would also be pulled down, and the boosting efficiency would be affected. Therefore, the predictive power of solar panels under the condition of the cut-off voltage of batteries can be formulated by Eq. (25).

$$P_{\max,k+L}^{sout} = \min\left(P_{\max,k+L}^{l} - P_r \lambda_1 \right) \lambda_2 \tag{25}$$

where $P_{max.k+L}^{l}$ denotes the peak generation power of solar panels during the timeslots $\Delta t = L \times T_s$ and P_r is the current generation power. λ_1 represents the factor on the generation power of solar panels when the battery voltage drops to the cut-off voltage. λ_2 represents the booster efficiency of MPPT. According to the experimental validation, the values of λ_1 and λ_2 are determined as 0.91 and 0.93, respectively.

3.3 Maximum power prediction

The proposed available maximum power prediction mainly contains two sections: 1) SOP

derivation based on the SOC estimation, and 2) the correction of SOP considering solar panels.

3.3.1 SOP derivation based on SOC estimation

The SOP prediction algorithm includes the terminal voltage estimation, SOC constraints, and maximal current constraints. To make the terminal voltage estimation more accurate, the second-order RC model to estimate the terminal voltage as defined by Eq. (26).

$$U_{L,k+L} = U_{OC}\left(z_{k+L}, Q_N\right) - U_{1,k+L} - U_{2,k+L} - R_i \cdot i_{k+L} \tag{26}$$

where z_k denotes the battery SOC, which is the function of current i_k. Through the decoupling control of battery SOC and open circuit voltage, the terminal voltage at any timeslot is estimated. Considering the length of this paper, the derivation of the estimation of terminal voltage has been attached in **Appendix A.3**.

$$
\begin{aligned}
U_{L,k+L} = U_{OC}\left(z_k, Q_N\right) - \frac{i_k \eta L T_s}{Q_N} \frac{\partial U_{OC}}{\partial z}\bigg|_{Z=Z_k} &- \left[\left(e^{-\frac{T_s}{\tau_1}}\right)^L U_{1,k} + i_k R_1\left(1 - e^{-\frac{T_s}{\tau_1}}\right)\Sigma_{j=0}^{L-1}\left(e^{-\frac{T_s}{\tau_1}}\right)^{L-1-j} \right. \\
&\left. + \left(e^{-\frac{T_s}{\tau_2}}\right)^L U_{2,k} + i_k R_2\left(1 - e^{-\frac{T_s}{\tau_2}}\right)\Sigma_{j=0}^{L-1}\left(e^{-\frac{T_s}{\tau_2}}\right)^{L-1-j} \right] - R_i \cdot i_k
\end{aligned}
\tag{27}
$$

The upper and lower cut-off terminal voltages is marked as $U_{L,max}$ and $U_{L,min}$, and the corresponding maximum allowable currents in the charge and discharge processes $I_{min,k+L}^{chg,V}$ and $I_{min,k+L}^{dis,V}$ can be obtained by Eq. (28).

$$
\begin{cases}
i_{\min,k+L}^{chg,V} = \dfrac{U_{OC}(z_k,Q_N) - \left(e^{-\frac{T_S}{\tau_1}}\right)^L U_{1,k} - \left(e^{-\frac{T_S}{\tau_2}}\right)^L U_{2,k} - U_{L,\max}}{\dfrac{\eta L T_s}{Q_N}\left.\dfrac{\partial U_{OC}}{\partial z}\right|_{Z=Z_k} + R_1\left(1-e^{-\frac{T_s}{\tau_1}}\right)\Sigma_{j=0}^{L-1}\left(e^{-\frac{T_s}{\tau_1}}\right)^{L-1-j} + R_2\left(1-e^{-\frac{T_s}{\tau_2}}\right)\Sigma_{j=0}^{L-1}\left(e^{-\frac{T_S}{\tau_2}}\right)^{L-1-j} + R_i} & (28a) \\[4em]
i_{\max,k+L}^{dis,V} = \dfrac{U_{OC}(z_k,Q_N) - \left(e^{-\frac{T_S}{\tau_1}}\right)^L U_{1,k} - \left(e^{-\frac{T_S}{\tau_2}}\right)^L U_{2,k} - U_{L,\min}}{\dfrac{\eta L T_s}{Q_N}\left.\dfrac{\partial U_{OC}}{\partial z}\right|_{Z=Z_k} + R_1\left(1-e^{-\frac{T_s}{\tau_1}}\right)\Sigma_{j=0}^{L-1}\left(e^{-\frac{T_s}{\tau_1}}\right)^{L-1-j} + R_2\left(1-e^{-\frac{T_S}{\tau_2}}\right)\Sigma_{j=0}^{L-1}\left(e^{-\frac{T_S}{\tau_2}}\right)^{L-1-j} + R_i}
\end{cases}
$$

(28b)

The SOC constraints is to limit the overcharge or over-discharge conditions. When the SOC approaches to the safety threshold, the maximal charging and discharging currents are depicted by Eq. (29).

$$
\begin{cases}
i_{\min,k+L}^{chg,Z} = \dfrac{Z_k - Z_{\max}}{L\eta T_s / Q_N} & (29a) \\[1.5em]
i_{\max,k+L}^{dis,Z} = \dfrac{Z_k - Z_{\min}}{L\eta T_s / Q_N}
\end{cases}
$$

(29b)

where $i_{min,k+L}^{chg,Z}$ and $i_{max,k+L}^{dis,Z}$ denote the maximum charging and discharging currents with SOC constraints, respectively. Z_{min} and Z_{max} represent the lower and upper boundaries of SOC values, respectively. Considering that when the SOC is lower than 0.1, the battery model is not accurate, the value of Z_{min} and Z_{max} are determined as 0.1 and 1, respectively. Honestly, this value can be adjusted according to the practical application.

In summary, the peak current can be determined by Eq. (30), among which constraints of Eq. (28) and Eq. (29) is utilized.

$$
\begin{cases}
i_{\min}^{chg} = \max\left\{i_{\min}, i_{\min,k+L}^{chg,V}, i_{\min,k+L}^{chg,Z}\right\} & (30a) \\[1em]
i_{\max}^{dis} = \min\left\{i_{\max}, i_{\max,k+L}^{dis,V}, i_{\max,k+L}^{dis,Z}\right\}
\end{cases}
$$

(30b)

where i_{min} and i_{max} represent the minimum and maximum charging and discharging designed limits. i_{min}^{chg} and i_{max}^{dis} are the maximum continuous charging and discharging currents, respectively. Accordingly, the continuous peak power can be expressed by Eq. (31) with the terminal voltages and allowed peak currents.

$$\begin{cases} P_{min}^{chg} = U_{L,k+L} i_{min,k+L}^{chg} \end{cases} \tag{31a}$$

$$P_{max}^{dis} = U_{L,k+L} i_{max,k+L}^{dis} \tag{31b}$$

where P_{min}^{chg} and P_{max}^{dis} denote the maximum charging and discharging power. Substituting Eq. (27) into Eq. (31), the real-time peak power can be predicted by Eq. (32).

$$\begin{cases} P_{min}^{chg} = i_{min,k+L}^{chg} \left(\begin{matrix} U_{OC}(z_k, Q_N) - \left[\left(e^{-\frac{T_s}{\tau_1}} \right)^L U_{1,k} + \left(e^{-\frac{T_s}{\tau_2}} \right)^L U_{2,k} \right] \\ -i_{min,k+L}^{chg} \left[\begin{matrix} \frac{\eta L T_s}{Q_N} \frac{\partial U_{OC}}{\partial z}\Big|_{Z=Z_k} + R_2 \left(1 - e^{-\frac{T_S}{\tau_2}}\right) \Sigma_{j=0}^{L-1} \left(e^{-\frac{T_S}{\tau_2}} \right)^{L-1-j} \\ +R_1 \left(1 - e^{-\frac{T_s}{\tau_1}}\right) \Sigma_{j=0}^{L-1} \left(e^{-\frac{T_s}{\tau_1}} \right)^{L-1-j} + R_i \end{matrix} \right] \end{matrix} \right) \tag{32a} \end{cases}$$

$$P_{max}^{dis} = i_{max,k+L}^{dis} \left(\begin{matrix} U_{OC}(z_k, Q_N) - \left[\left(e^{-\frac{T_s}{\tau_1}} \right)^L U_{1,k} + \left(e^{-\frac{T_s}{\tau_2}} \right)^L U_{2,k} \right] \\ -i_{max,k+L}^{dis} \left[\begin{matrix} \frac{\eta L T_s}{Q_N} \frac{\partial U_{OC}}{\partial z}\Big|_{Z=Z_k} + R_2 \left(1 - e^{-\frac{T_S}{\tau_2}}\right) \Sigma_{j=0}^{L-1} \left(e^{-\frac{T_S}{\tau_2}} \right)^{L-1-j} \\ +R_1 \left(1 - e^{-\frac{T_s}{\tau_1}}\right) \Sigma_{j=0}^{L-1} \left(e^{-\frac{T_s}{\tau_1}} \right)^{L-1-j} + R_i \end{matrix} \right] \end{matrix} \right) \tag{32b}$$

According to the above derivations, the illustration of SOP prediction is depicted in **Fig. 4(c)**. The details are described by six major steps as follows.

Step (1): The parameters regarding the battery voltages, currents and the temperature are initialized and used in the look-up tables.

Step (2): Update the model deviation time.

Step (3): Calculate the Kalman gain in the EKF algorithm.

Step (4): Based on the priori terminal voltage, calculate its posterior value with Kalman gain and then get the SOC and polarisation voltage U_p.

Step (5): Calculate the peak currents constrained by single cell voltage and SOC.

Step (6): Calculate the peak power with Eq. (31) and finish the joint SOP prediction and SOC estimation.

3.3.2 SOP Correction based on the generation power of solar panels

Theoretically, the power battery pack relates to the solar panel array in parallel. The peak current of power battery pack should be the integration of all parallel cell units by Eq. (33).

$$
\begin{cases}
P_{min,mod}^{chg} = n_p \sum_{m=1}^{ns} i_{min,k+L}^{chg} U_{k,m}(k+L) & \text{(33a)} \\
P_{max,mod}^{dis} = n_p \sum_{m=1}^{ns} i_{max,k+L}^{dis} U_{k,m}(k+L) & \text{(33b)}
\end{cases}
$$

where $P_{min,mod}^{chg}$ and $P_{max,mod}^{dis}$ represent the peak charging and discharging power of battery pack, respectively. n_p denotes the number of parallel connections of cells. According to the description in **Section 3.1**, the total peak power of battery pack can be expressed by Eq. (34).

$$
\begin{cases}
P_{bat}^{chg} = \left| P_{min,mod}^{chg} + P_{max,k+L}^{sout} \right| & \text{(34a)} \\
P_{bat}^{dis} = P_{max,mod}^{dis} + P_{max,k+L}^{sout} & \text{(34b)}
\end{cases}
$$

where the peak charging power of battery pack $P_{min,mod}^{chg}$ behaves negative. P_{bat}^{chg} denotes the allowed maximum power when the braking energy is recovered, which is the sum of maximum solar panel array power $P_{max,k+L}^{sout}$ and the allowed peak charging power $P_{min,mod}^{chg}$.

The experimental results of SOP prediction with multiple parameters are shown in **Fig. 4(d)** and **(e)**. As illustrated in **Fig. 4(d)**, the discharge of batteries enables the SOC decreases and thereby the available peak charging power is increased. However, at time 7885-9882s, the predictive current exceeds the designed value; therefore, the predictive peak power remains constant. Then, the terminal voltage constraints start to work and enables the predictive current decrease, resulting in the decrease of peak discharge power. The predictive discharging power is illustrated in **Fig. 4(e)**. At the start stage of 0-6408s, the predictive charge currents keep stable and after then, the voltage constrains the peak discharge power. When the SOC approaches to 0.1, the predictive current with the SOC constraints drops dramatically, which enables the discharge power to quickly decrease to avoid the over-discharge conditions.

4 Optimal charging strategy

Another significant role of the proposed BMS is to optimize the charging process. Since the lessening of charging time benefits to the labour cost and charging efficiency, the optimization of charging time is selected as one important objective. Nevertheless, the pursuit of lessening charging time will inevitably cause a large charging current, which would incur the uncontrollable temperature rise, affecting the charging performance and damaging the lithium battery. Thus, the temperature rise is also regarded as the second objective. Generally, this section aims at optimizing the charging current in the multi-stage charging strategy to reduce the charging time in the premise of maintaining the controllable temperature rise. Concretely, the designed charging strategy divides different charging intervals according to the different SOC values. Corresponding charging current in each interval is optimized by the adaptive GA

approach.

Two sub-objectives of the temperature rise and charging time are considered in this strategy as defined in Eq. (35a) subject to a series of constraints of Eq. (35b). Thus, the overall optimization objective is the weighted-sum of the two sub-objectives.

$$\begin{cases} F_{obj} = \alpha t + \beta \Delta T \\ \Delta T = T_{max} - T_{init} \end{cases} \tag{35a}$$

$$\text{s.t.} \quad \begin{cases} U_k \leq U_{max} \\ 0 \leq I_k \leq I_{max} \\ T < T_{max} \\ SOC_{final} = 90\% \\ t_{chg} < t_{cc} \end{cases} \tag{35b}$$

where α and β denote the weighted factors corresponding to the charging time and temperature rise; they satisfy $\alpha + \beta = 1$. t denotes the charging duration and ΔT denotes the temperature rise, which has been modelled in **Section 2.3**. $U_{max} = 4.2V$ is the upper cut-off voltage of batteries; $I_{max} = 1C$ denotes the allowed peak current; $T_{max} = 45°C$ denotes the maximum allowed temperature; $SOC_{final} = 90\%$ is the final charging SOC. In this study, the allowed charging SOC range in the optimization is 0-90% and each SOC interval adopts 10%.

Since the charging time and temperature rise during each charging interval vary with the optimization processing, the weighting factor of α and β should be adaptively regulated. In this study, the ultimate current value (UCV) is selected as the criteria to allocate the weighted factors since the UCV can represent the internal characteristics of batteries. The UCV can be calculated with the maximum terminal voltage as expressed by Eq. (36).

32

$$I_{\text{limit}}(SOC) = \frac{U - U_{oc}(SOC) - U_1(SOC) - U_2(SOC)}{R(SOC)}$$

$$= \frac{4.2 - U_{oc}(SOC) - U_1(SOC) - U_2(SOC)}{R(SOC)} \tag{36}$$

where $U_{OC}(SOC)$, $U_1(SOC)$, $U_2(SOC)$ and R(SOC) represent the open-circuit voltage, polarization voltage 1, polarization voltage 2, and the battery internal resistance. Considering the parametric model in **Section 2**, the UCV in each SOC interval can be obtained. The UCV can reflect the charging time. The UCV can be changed proportionally to characterize the value of α in the corresponding SOC intervals. Accordingly, the final weighting factor has been determined by Eq. (37).

$$\begin{cases} \alpha + \beta = 1 \\ \alpha : \beta = 7 : 3 (0 \leq SOC \leq 0.2) \\ \alpha : \beta = 4 : 6 (0.2 < SOC \leq 0.6) \\ \alpha : \beta = 4 : 6 (0.6 < SOC \leq 0.9) \end{cases} \tag{37}$$

After obtaining the objective and adaptive weighting factors, the charging current in each interval can be optimized by using GA[32]. Briefly, the total GA based charging algorithm is depicted as the following major steps.

Step (1): Determine the objectives and constraints with Eq. (35);

Step (2): Determine the adaptive weighting factors with Eq. (37);

Step (3): Code the charging current ratio with the binary coding. The charging current ratio is limited within 0.2-1.0C and its accuracy selects 0.001C. In this way, the o.1C is regarded as a population, in which 100 individuals are included.

Step (4): Design the fitness function. To uniformly measure the both objectives, the normalization of two objectives is executed as defined by Eq. (38).

$$F_{obj} = \alpha \frac{t - t_{\min}}{t_{\max} - t_{\min}} + \beta \frac{\Delta T - \Delta T_{\min}}{\Delta T_{\max} - \Delta T_{\min}} \tag{38}$$

where t_{min} and t_{max} are the minimum and maximum charging time; ΔT_{min} and ΔT_{max} are

the minimum and maximum temperature rise, which corresponds to the temperature rise with

1.0C and 0.2C charging currents. Therefore, the fitness function is defined by Eq. (39).

$$\begin{cases} F(\mathrm{x}) = a \cdot F_{obj} + \mathrm{b} \\ a = \dfrac{2}{F_{obj_{\min}} - F_{obj_{\max}}} \\ b = \dfrac{2F_{obj_{\min}}}{F_{obj_{\max}} - F_{obj_{\min}}} + 2 \end{cases} \tag{39}$$

The boundary of fitness function ranges between 0 and 2. $F_{obj_{max}}$ and $F_{obj_{min}}$ are the

maximum and minimum values of the objective.

Step (5): Genetic operation. The genetic operation includes three functions, such as selection,

crossover and mutation. In this study, the random selection is applied and the multipoint

crossover algorithm is utilized. The mutation is to generate a new individual to avoid the local

optima.

So far, the desired charging current in the multi-stage conditions can be obtained with the

proposed charging strategy. In the practical charging process, the charger of electrical grid and

solar panels are coordinated to complete the charging task. During every control period, the total

desired charging current can be calculated. With the sampled current provided by the solar

panels, remaining charging current is provided by the grid charger.

5 Results and discussions

The proposed BMS was comprehensively validated using the practical experimental platform,

which combined the photovoltaic cells with the lithium multi-pack battery in a solar-assisted EV as shown in Fig. 5. The corresponding prediction and optimization strategies are programmed in the BMS control unit. On this basis, the maximum power prediction strategy and the optimal charging strategy are respectively evaluated and validated.
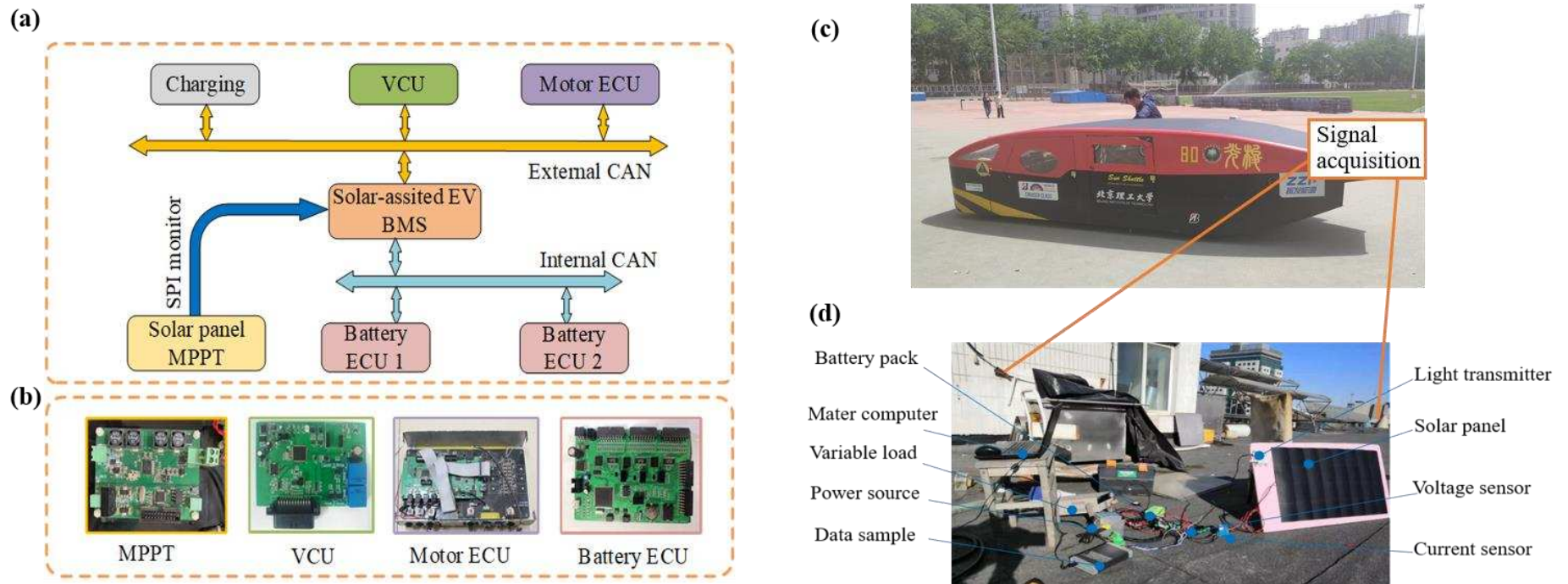
Fig. 5 Experimental platform of the solar-assisted EV. (a) Framework of the BMS; **(b)** The sub-system controllers; **(c)** The solar-assisted EV; **(d)** The signal

acquisition system.

5.1 Experimental setup

In the experiment, the BMS adopts the dual-loop communication network in which two sets of CAN networks are used for the communication between the master BMS controller and slaver controllers, as shown in **Fig. 5(a)** and **(b)**. Explicitly, the external CAN network is responsible for the BMS communication with the battery charger, electrical signal sample, and power up-down management. The internal CAN network enables the BMS to communicate with the battery ECU. As for the physical structure, a solar-assisted EV is equipped with the signal acquisition system as shown in **Fig. 5(c)** and **Fig. 5(d)**. Both the lithium battery and the solar panels provide electricity to the driving motors of the EV. The battery pack and solar panels are connected in parallel to provide the electricity to the variable resistant load. The voltage and current signals of solar panels, output current of MPPT, battery voltage, are sampled with the electrical sensors, which are transferred to digital signals for the algorithm utilization. The available solar energy is collected with the light transmitter devices and the radiation intensity is thereby determined and utilized in the MPPT algorithm. Accordingly, all sample information is monitored by the PC master with CAN networks.

5.2 Validation of the maximum power prediction strategy

To test the adaptability of solar panels and MPPT system, a group of variant loads is set up as presented in **Table 2**. A group of loads operates for 400s with the separative 10s standing time (Step 3), during which the power battery is charged with solar panels. Besides, the hybrid discharging mode with different discharge power is available in other durations, which enlarges

the power output of multi-pack battery and amplify the variation trend of the battery SOC.

The power loads, solar generation power, and battery power are presented in **Fig. 6**. The open-circuit voltage is set as 24.4 V and the entire test condition includes 17 single cycles (one cycle is displayed in **Table 2**). From the view of **Fig. 6(b)**, the power of solar panels is stable almost without fluctuations when the SOC is larger than the allowance value 0.1, which manifests that the generation power of solar panels is not affected by the variant loads. After then, the generated power shows a larger fluctuation, which is caused by the variant battery voltage with lower SOC value less than 0.1. Overall, the average generated power of panels is 91.2 W and the average boosting efficiency of MPPT device is up to 94.29%. The converted energy is 602.7 kJ, and the battery output energy is 231.2 kJ. The battery pack provides 27.8% of total consumed energy while the solar panels fulfil 72.2% energy demands.

To validate the effectiveness of the proposed predictive generation power algorithm of solar

Table 2 Variable load description of one cycle.

| Step	Power (W)	Time (s)
1	110	120
2	120	60
3	0	10
4	120	100
5	145	100
6	0	10

panels, we make a comparison with the actual measured generation power as presented in **Fig. 6**. The predictive generated power can well follow the change of the actual generated power and the predictive error is lower than 2W, which is profited from that the proposed predictive algorithm is not significantly affected by the variant battery voltage.
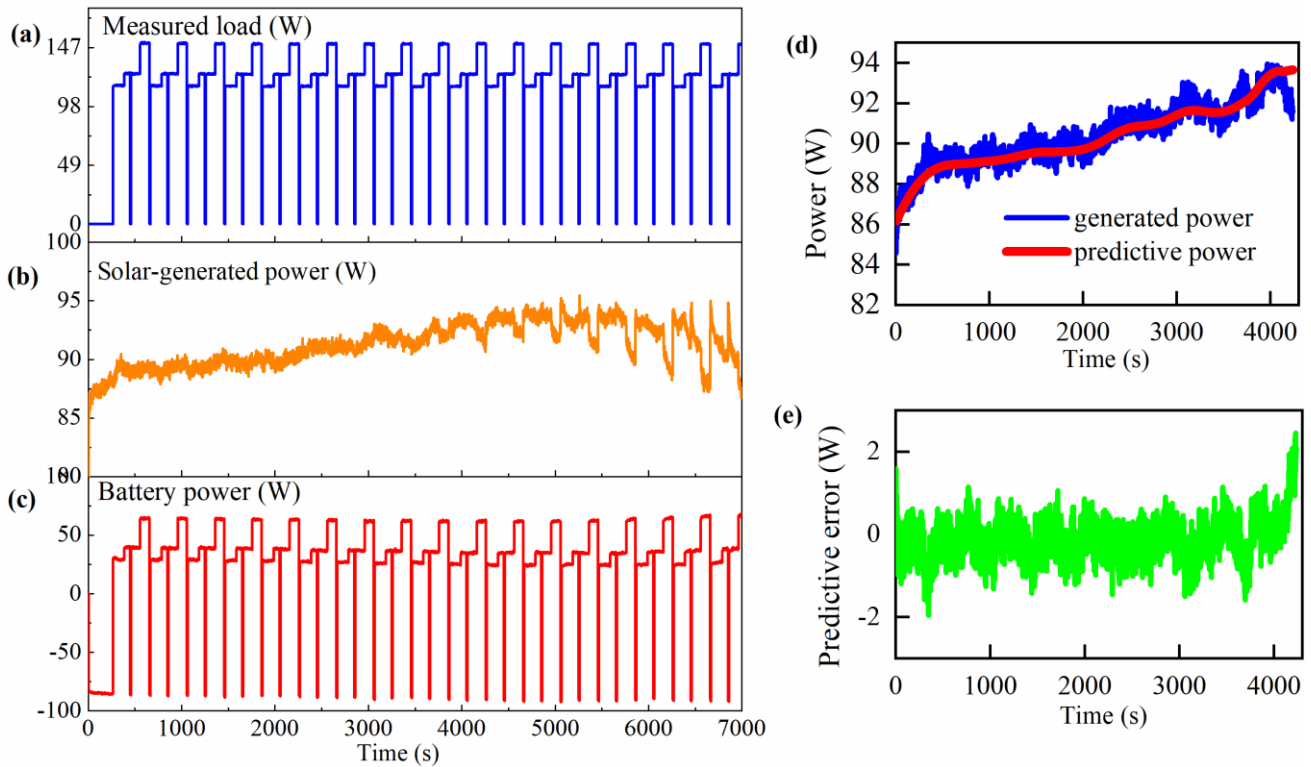
Fig. 6 SOP results of the battery system. (a) Measured load; **(b)** solar-generated power; **(c)** battery power; **(d)** comparison of the predictive and generated powers; **(e)** predictive power error between predictive and generated powers.

The change of SOC value and the resulting SOP value are illustrated in **Fig. 7**. From the **Fig. 7(a)**, the initial SOC is sampled as 0.222, and after 17 operating cycles, the final SOC is lower than 0.017, which indicates that the battery pack is approaching to the full discharge. The peak generated power of solar panels shown in **Fig. 7(b)** is lower than the predictive generated power due to the impact of the peak voltage drop. The predictive peak charging power of the battery pack is presented in **Fig. 7(c)** and **(d)**. Considering that excessive peak currents in the lower battery state would impair the battery pack, when the battery SOC decreases less than 0.1, the peak operating power would be constrained as zero in the SOP predictive algorithm. When the battery SOC value varies between 0.222 and 0.1, the predictive power in the SOP algorithm tends
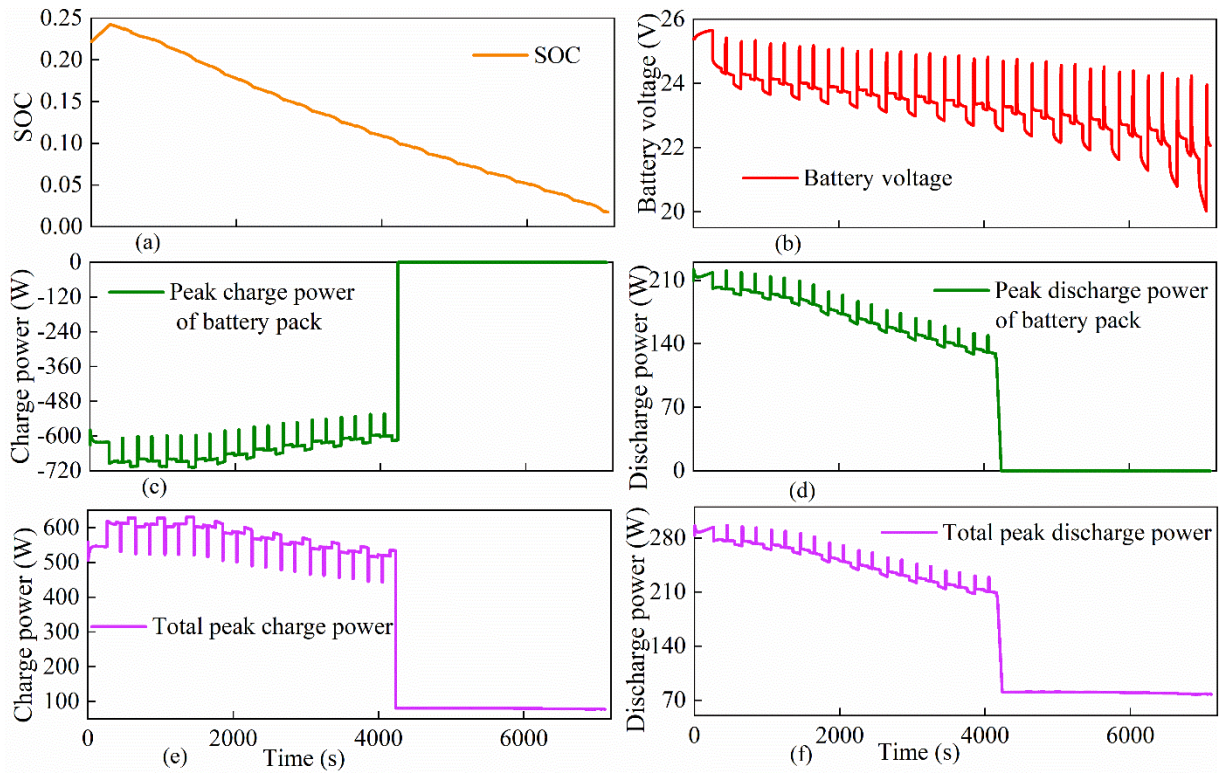
Fig. 7 The predictive results of the battery power and the total BMS.

to decrease, which results in the increase of peak power for the battery pack and the solar panels as shown in **Fig. 7(e)** and **(f)**, respectively. After comprehensively considering the maximal power, the increasing peak power of battery pack would promote the discharging limit, extending the travelling distance of the traditional EVs.

5.3 Validation of the optimal charging strategy

The accuracy and adaptability of the designed multi-stage constant current charging algorithm are validated as well. Two different charging situations of charging ratios and initial SOC values are particularly studied. Meanwhile, the traditional single constant current charging mode is utilized as a benchmark for comparison purpose.

5.3.1 Impact of charging ratios on the charging performance

Three different charging ratios, i.e. 0.3C, 0.5C and 0.8C, are setup and the charging

performance is listed in **Table 3**. It is seen that the designed multi-stage constant current

charging mode in the 0.3C charging ratio condition would decrease the total charging time by

Table 3 Charging performance evaluation of different charging ratios.

Charging ratios	Traditional constant current mode		Designed multi-stage constant current mode		Optimization	
	Charging time	Temperature rise	Charging time	Temperature rise	Charging time	Temperature rise
0.3C	11693s	3.94℃	10631s	2.55℃	9.08%	35.27%
0.5C	7292s	7.51℃	6717s	4.45℃	7.14%	40.75%
0.8C	4568s	9.76℃	4056s	6.05℃	11.21%	38.01%

1062s and reduce the temperature rise by 1.39℃, which indicates that the charging performance

is improved. Furthermore, the charging time in the 0.5C and 0.8C conditions is improved by 7.14%

and 11.21%, respectively. The maximum temperature rises in the 0.5C and 0.8C conditions have

been improved by more than 35%, which implies that the temperature rise has been effectively

controlled by the designed charging strategy. With the increase of charging ratios from 0.3C to

0.8C, the charging time is reduced but the temperature rise has been effectively optimized. This

is because the designed charging strategy can dynamically regulate the charging currents and

further constrain the battery polarisation voltage. The different charging current in the adjacent

SOC regions can well optimize the heat produced by the battery properly. Compared with the

benchmark, the proposed multi-stage constant current charging mode significantly reduces the

energy depletion and further protect the battery pack.

5.3.2 Impact of initial SOC values on charging performance

To validate the adaptability of charging strategy, three different initial SOC values, 10%, 40%,

and 60%, are adopted to simulate the random charging behaviours. In this test, the charging ratio

0.5C is employed. The preparatory works starts from charging the battery to the targeted initial

SOC values with 10%, 40% and 60%, respectively. Then, all pack batteries are placed for 1h to

stabilize the battery temperature. Then, the battery is charged to 90% of SOC values with the

designed charging strategy, and the results regarding the electrical parameters and temperature

rise are depicted in **Fig. 8** and **Table 4**, respectively. From **Fig. 8(a)**, the charging ratio can be

adaptively regulated in adjacent SOC intervals, and the final battery voltage approaches to about

4.2V, which indicates that the designed multi-stage charging mode can effectively handle the

charging task in the premise of the controllable temperature rise. In addition, from the charging

curves with different initial SOC values, the charging current can be adaptively adjusted, which
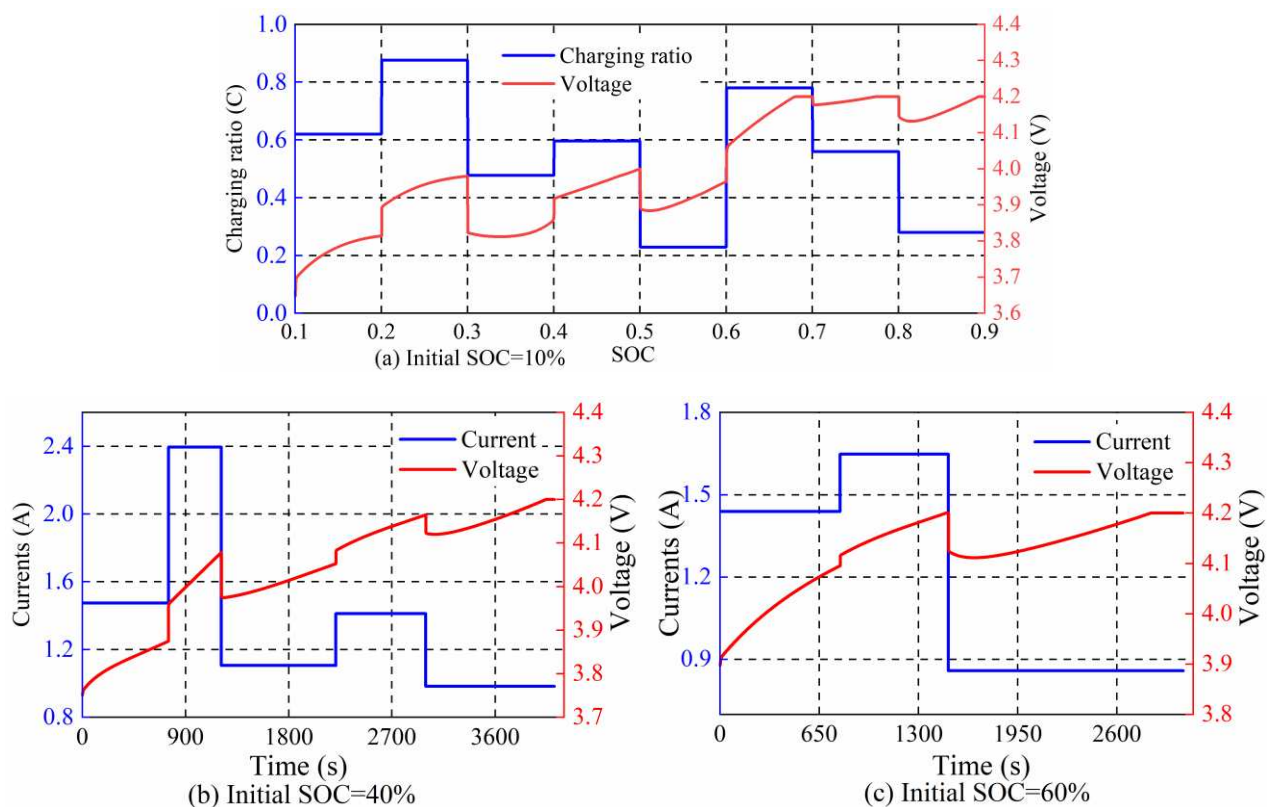
Fig. 8 Optimal charging results under different initial SOC values. (a) Initial SOC=10%; **(b)** initial SOC=40%;

(c) initial SOC=60%.

42

also implies that the designed charging strategy is robust to different initial battery states.

Table 4 quantifies the advantages of the designed optimal charging strategy. Compared with the benchmark, the designed optimal multi-stage charging strategy achieves less charging time by 6.62%~9.70% and the maximal temperature rise can be reduced by over 40%. With the increase of initial SOC, the total charging time and temperature rise have been significantly improved. According to these results, the proposed charging strategy can charge the battery much faster with lower temperature rise than the traditional strategy, implying less energy loss.

Table 4 Charging performance evaluation of different initial SOC values.

Initial SOC	Traditional charging method		Proposed charging method		Optimization	
	Charging time	Temperature rise	Charging time	Temperature rise	Charging time	Temperature rise
10%	6613s	7.48℃	6147s	4.24℃	7.04%	43.32%
40%	4304s	6.21℃	4019s	3.48℃	6.62%	43.96%
60%	3218s	5.68℃	2906s	3.35℃	9.70%	41.02%

6 The way forward

1) The charging mode selection should be further studied with the application of photovoltaic cells. Constant voltage charging mode has also been studied by scholars from the perspective of higher charging efficiency [22, 35] However, the electromotive force of the batteries is lower in the initial charging stage, which would result in the larger charging current and impair the battery health. Therefore, a significant direction lies in the charging mode selection aiming at collaborative research of higher charging efficiency and battery health.

2) The decarbonization of transport sector requires more studies towards green energy. Therefore, the future research direction may focus on the multi-source energy application such

as solar energy, fuel cells, and hydrogen hybrid engines. Besides, the collaborative charging control strategy between these renewable energy requires more attention.

7 Conclusion

The solar-assisted EV is expected to extend the EVs driving mileage in a sustainable manner. To address the challenge of coordinating vehicle-roof solar panels and the lithium battery system, a customized BMS for the solar-assisted EV is proposed and validated in this study. This BMS mainly consists of three modules. Firstly, the second-order RC model and solar panel conversion model are established. On this basis, the EKF-AH algorithm is designed to estimate the SOC in the whole intervals and the maximum available power for the solar-assisted EV predicted considering the generation power of solar panels. Accordingly, the last module of multi-stage constant current charging strategy is developed based on the GA method, in which the temperature rise and charging time are both optimized. The whole BMS is tested by the hardware experimental test, leading to the following findings.

(1) The proposed parameter identification algorithm based on the improved RLS method couples the large time constant and internal resistance as the constraint factors to address the problem of differential constant of RC links. Results indicates that the estimated terminal voltage error is less than 20mV under the HPPC condition.

(2) The issue of inaccurate estimation of SOC in the low SOC intervals can be addressed by the proposed EKF-AH algorithm; the joint estimation method can reduce the SOC estimation error within 0.01 under the constant 0.3C discharging condition.

(3) The hardware experiment reveals that the radiation intensity has a higher impact on the

generation power than the temperature. The average boosting efficiency of solar panels is up to 96.29% and the predictive generation power error is less than 1 %.

(4) The proposed battery temperature rise model and thermal dynamics model turn out effective. Among which the developed multi-stage constant charging optimization algorithm achieve less charging time and lower maximal battery temperature than the traditional single-stage constant charging algorithm.

In the future, the proposed BMS modelling framework can be further extended to combine with the vehicle driving cycles. Meanwhile, the SOH in the BMS should be further studied to optimize the battery aging performance.

Acknowledge

Declaration of interest

There are no conflicts to declare.

Appendix

This appendix describes the offline battery experiment in **Appendix A.1**, the SOC estimation algorithm in **Appendix A.2** and the formulation derivation of SOP constraints in **Appendix A.3**.

A.1 Offline battery experiment

The battery characteristics play a significant role in the parameter identification and algorithm design. From this point of view, we establish a set of the experimental platforms to test the battery characteristics as shown in **Fig. A1** (All figures in the **Appendix** part are illustrated in **Supplement Documents**). The battery test platform utilizes the ITS5300 test system (ITECH corporation) to execute the constant current charging and discharging test, constant power discharging test and constant resistance discharging test, in which the IT6832 and IT8511A+ are utilized to provide the programmable DC power supply and loads. The K-type thermocouple is pasted on the surface of the battery to sample its temperature during the charging and discharging process.

Fig. A2 depicts the battery capacity illustration with the discharging ratio and the temperature. With the increase of discharge ratio, the battery capacity is reduced; besides, the temperature also makes an effect on the actual battery capacity. The temperature is located within 25℃-40℃, the capacity with 1.5C discharging ratio is larger than 3000mAh, which implies that the battery has the good discharging performance.

Fig. A3 describes the temperature rise in the charge and discharge operations, respectively. When the discharge ratio is lower than 0.5C, the temperature rise is well controlled within 10℃ regardless of the initial surface temperature. When the basic temperature is higher than 45℃, the temperature rise rate is higher, and the temperature rise is up to 33.7℃ when the discharge ratio is 1.5C. Similarly, the temperature rise in the charge conditions presents a similar tendency. When the initial temperature is higher than 45℃, there is a risk with losing control.

Fig. A4 describes the open-circuit voltage (OCV) curves with the different SOC values and temperatures. The higher temperature denotes the larger open-circuit voltage range. Taking the average value of the charge and discharge OCV corresponding to different SOC intervals at each temperature point, the data (see **Table A1**) obtained can be used to fit the empirical formula of the OCV.

Table A1 The OCV parameters under different temperatures and SOC values.

Temperature	0	10%	20%	30%	40%	50%	60%	70%	80%	90%	100%
15℃	3.323	3.437	3.531	3.582	3.630	3.695	3.798	3.873	3.945	4.041	4.151
25℃	3.292	3.399	3.518	3.579	3.621	3.689	3.800	3.884	3.969	4.071	4.174
35℃	3.199	3.373	3.501	3.567	3.615	3.672	3.785	3.863	3.947	4.054	4.153
45℃	3.108	3.352	3.476	3.561	3.613	3.673	3.778	3.862	3.943	4.051	4.176

The final OCV-SOC curve is illustrated in **Fig. A5**. When SOC is larger than 0.2, the OCV is almost similar; however, when SOC is lower than 0.2, the OCV significantly varies with temperatures. In this study, OCV values are fitted with eighth order expression as expressed in Eq. (A1) and the coefficients are listed in **Table A2**. The mean absolute error is 0.0027 and the root mean square error is 0.004.

$$
\begin{aligned}
f(OCV) = {} & k_8 SOC^8 + k_7 SOC^7 + k_6 SOC^6 + k_5 SOC^5 + k_4 SOC^4 \\
& k_3 SOC^3 + k_2 SOC^2 + k_1 SOC + k_0
\end{aligned}
\tag{A1}
$$

where k_1-k_8 is the fitting factors.

Table A2 Fitting factor definition with the different temperatures.

Coefficients	15℃	25℃	35℃	45℃

k_8	-128.1850	-109.2575	-205.3310	-341.2176
k_7	432.4414	332.8634	732.2135	1332.8911
k_6	-543.6812	-326.8974	-1014.8166	-2108.5956
k_5	297.1311	44.4201	679.1413	1736.9305
k_4	-49.5682	119.3213	-218.9950	-802.1044
k_3	-11.0741	-74.6393	30.3223	212.7218
k_2	2.7655	14.8656	-3.5295	-33.9058
k_1	0.9986	0.2056	1.9490	4.3480
k_0	3.3230	3.2920	3.1990	3.1080
MAE	0.0016	0.0018	0.0027	0.0018
RMSE	0.0024	0.0027	0.004	0.0027

A.2 SOC estimation strategy

How to accurately estimate the SOC is vital for the vehicle operation. However, in practice, a larger estimation error often exists when the battery SOC is lower than 10% especially for the second-order RC battery model. The reason is that the battery model may be distorted in such a case [33]. To address this problem, an accurate estimation algorithm is proposed by combining the EKF and AH algorithms.

According to Eq. (1), U_1, U_2 and *SOC* are selected as state variables. The discrete state-space equation can be expressed by Eq. (A2).

$$x_k = \begin{bmatrix} U_{1,k} \\ U_{2,k} \\ SOC_k \end{bmatrix} = \underbrace{\begin{bmatrix} e^{-T/\tau_1} & 0 & 0 \\ 0 & e^{-T/\tau_2} & 0 \\ 0 & 0 & 1 \end{bmatrix}}_{A_k} \begin{bmatrix} U_{1,k-1} \\ U_{2,k-1} \\ SOC_{k-1} \end{bmatrix} + \underbrace{\begin{bmatrix} R_1\left(1-e^{-T/\tau_1}\right) \\ R_2\left(1-e^{-T/\tau_2}\right) \\ -\dfrac{T}{C_0} \end{bmatrix}}_{B_k} I_{k-1} + \begin{bmatrix} w_{1,k-1} \\ w_{2,k-1} \\ w_{3,k-1} \end{bmatrix} \tag{A2}$$

where w_1, w_2, and w_3 are system noises, which are disturbance variables. The system output is expressed by Eq. (A3).

$$y_k = U_k = C_k \begin{bmatrix} U_{1,k} \\ U_{2,k} \\ SOC_k \end{bmatrix} - R_0 I_k + U_{oc} + v_k \tag{A3}$$

where $C_k = \frac{\partial U}{\partial x_k} = \begin{bmatrix} \frac{\partial U}{\partial U_1} & \frac{\partial U}{\partial U_2} & \frac{\partial U}{\partial SOC} \end{bmatrix} = \begin{bmatrix} -1 & -1 & \frac{\partial U_{oc}}{\partial SOC} \end{bmatrix}$. The open-circuit voltage U_{oc} is the eighth-order polynomial approximation as expressed in Eq. (A1), and $\frac{\partial U}{\partial SOC}$ can be solved by Eq. (A4).

$$\frac{\partial U_{oc}}{\partial SOC} = a_1 + 2a_2 z^1 + 3a_3 z^2 + 4a_4 z^3 + 5a_5 z^4 + 6a_6 z^5 + 7a_7 z^6 + 8a_8 z^7 \tag{A4}$$

where z denotes the SOC and coefficients a_1-a_8 can be determined by looking up the **Table A2**.

With Eq. (A2) and Eq. (A3), the EKF algorithm can be applied to estimate the SOC value in real time. The details of EKF algorithm can refer to [34].

Although the EKF exhibits a good estimation performance when the SOC value is larger than 20%, the accuracy would be impaired under the condition of lower SOC. Therefore, this study introduces the AH algorithm to correct the SOC estimation for avoiding the over-discharge problem under lower SOC conditions. The AH method adopts the mathematical expression of Eq. (A5).

$$SOC(t) = SOC\left(t_0\right) - \int_{t_0}^{t} \frac{\eta I(t)\mathrm{d}t}{C_0} \tag{A5}$$

The joint estimation EKF-AH algorithm is described below. Assuming that the estimated SOC values in EKF method and AH are marked as SOC_1 and SOC_2, the final SOC estimation can be

expressed as their weighted-sum as derived by Eq. (A6).

$$SOC(k) = K(k)SOC_1(k) + [1 - K(k)]SOC_2(k) \qquad (A6)$$

where K denotes the weighted coefficient of EKF algorithm while 1-K denotes the weighted coefficient of AH algorithm. When the SOC is larger than 20%, the EKF algorithm can guarantee the higher accuracy; therefore $K = 1$ is selected. When the SOC value locates within range [0.1, 0.2], the ramped weighted coefficient is determined linearly. Other assumption of $K = 0$ occurs in the case of SOC < 10%. In summary, the allocation of weighted coefficient can be depicted by Eq. (A7).

$$K(k) = \begin{cases} 1 & SOC_1(k) \geq 0.2 \\ 10SOC_1(k) - 1 & 0.1 \leq SOC_1(k) < 0.2 \\ 0 & SOC_1(k) < 0.1 \end{cases} \qquad (A7)$$

We performed the experimental charging test under conditions of 0.3C charging ratio and DST test. The estimated results are illustrated in **Fig. A6(a)-(d)**. When the SOC is larger than 0.2, the EKF algorithm and joint estimated algorithm can both observe the actual SOC values. However, when the SOC decreases to be lower than 0.1, the EKF algorithm presents a larger estimation error while the designed joint estimation EKF-AH algorithm still shows high estimation performance.

To validate the robustness of the EKF-AH algorithm, the different initial SOC values are applied. A series of initial SOC errors ranging from 75% to 100% are set, and the estimation results and estimated error are expressed in **Fig. A6(e)-(f).** Explicitly, the estimation algorithm enables the estimation results to approach the actual values in despite of different initial SOC values. **Table A3** records the convergence of the EKF-AH algorithm under different initial SOC errors. The time

consumed when the explicit SOC error drops to 3%, 2.5%, and 2% for the first time is listed.

In the case of the most severe deviation of 75%, the initial error is as high as 23%. After 400s,

Table A3 Convergence of EKF-AH algorithm under different initial SOC values.

Initial SOC	Initial error	Error reduced less than 3%	Error reduced less than 2.5%	Error reduced less than 2%
95%	3%	1s	3s	5s
90%	8%	35s	48s	71s
85%	13%	244s	255s	475s
80%	18%	370s	523s	599s
75%	23%	400s	530s	610s

this error has dropped to less than 3%, and after 610s, this error has been less than 2%,

indicating that the designed EKF-AH algorithm can properly adapt to different SOC initializations.

A.3 Model voltage constraints in the SOP prediction

The model voltage constraint is a part of SOP prediction strategy. Assuming that the initial

operation timeslot is t_k and t_{k+L} denotes the timeslot after L samples, the terminal voltage

model in second-order RC model is expressed by Eq. (A8).

$$U_{L,k+L} = U_{OC}\left(z_{k+L}, Q_N\right) - U_{1,k+L} - U_{2,k+L} - R_i \cdot i_{k+L} \tag{A8}$$

Assuming that the battery excitation maintains constant within the continuous sample t_k-

t_{k+L}, $u_{k+L} = u_k$; the battery model is transferred as shown in Eq. (A9).

$$\begin{cases} x_{k+L} = A_{k+L}x_{k+L-1} + B_{k+L}u_{k+L-1} \\ y_{k+L} = C_{k+L}x_{k+L} + D_{k+L} \end{cases} \tag{A9}$$

Since the electrical parameters in the battery varies very slowly, therefore the battery

parameters during the peak power prediction period is regarded as constant by Eq. (A10).

$$x_{k+L} = A_k^L x_k + \left(\sum_{j=0}^{L-1} A_k^{L-1-j} B_k \right) u_k \tag{A10}$$

Considering the Eq. (6), the polarisation voltage during the peak power prediction period is formulated as Eq. (A11).

$$
\begin{aligned}
U_{P,k+L} &= U_{1,k+L} + U_{2,k+L} \\
&= \left(e^{-\frac{T_S}{\tau_1}} \right)^L U_{1,k} + i_{L,k} R_1 \left(1 - e^{-\frac{T_S}{\tau_1}} \right) \Sigma_{j=0}^{L-1} \left(e^{-\frac{T_S}{\tau_1}} \right)^{L-1-j} \\
&+ \left(e^{-\frac{T_S}{\tau_2}} \right)^L U_{2,k} + i_{L,k} R_2 \left(1 - e^{-\frac{T_S}{\tau_2}} \right) \Sigma_{j=0}^{L-1} \left(e^{-\frac{T_S}{\tau_2}} \right)^{L-1-j}
\end{aligned}
\tag{A11}
$$

Decoupling the OCV and currents with first-order Taylor expansion, the following equation of Eq. (A12) is depicted.

$$
\begin{aligned}
U_{OC}\left(z_{k+L}, Q_N \right) &= U_{OC}\left(z_k - \frac{\eta i_k L T_s}{Q_N}, Q_N \right) \\
&= U_{OC}\left(z_k, Q_N \right) - \frac{\eta L T_s}{Q_N} \left. \frac{\partial U_{OC}}{\partial z} \right|_{z=z_k} + \mathcal{R}_1\left(z_k, \frac{\eta L T_s}{Q_N} \right)
\end{aligned}
\tag{A12}
$$

Neglecting the higher order small quantities, the OCV formulation is derived as Eq. (A13).

$$U_{OC}\left(z_{k+L}, Q_N \right) = U_{OC}\left(z_k, Q_N \right) - \frac{\eta L T_s}{Q_N} \left. \frac{\partial U_{OC}}{\partial z} \right|_{z=z_k} \tag{A13}$$

Substituting Eq. (A11) and Eq. (A13) into Eq. (A8), the terminal voltage can be estimated by Eq. (A14).

$$
\begin{aligned}
U_{L,k+L} &= U_{OC}\left(z_k, Q_N \right) - \frac{i_k \eta L T_s}{Q_N} \left. \frac{\partial U_{OC}}{\partial z} \right|_{Z=Z_k} - \left[\left(e^{-\frac{T_s}{\tau_1}} \right)^L U_{1,k} + i_k R_1 \left(1 - e^{-\frac{T_s}{\tau_1}} \right) \Sigma_{j=0}^{L-1} \left(e^{-\frac{T_s}{\tau_1}} \right)^{L-1-j} \right. \\
&\left. + \left(e^{-\frac{T_s}{\tau_2}} \right)^L U_{2,k} + i_k R_2 \left(1 - e^{-\frac{T_s}{\tau_2}} \right) \Sigma_{j=0}^{L-1} \left(e^{-\frac{T_s}{\tau_2}} \right)^{L-1-j} \right] - R_i \cdot i_k
\end{aligned}
\tag{A14}
$$

Letting $U_{L,max}$ and $U_{L,min}$ denote the upper and lower cut-off voltages, the maximum charging and discharging currents would exist when the terminal voltage approaches to $U_{L,max}$ or $U_{L,min}$.

Therefore, the maximum charging and discharging currents $I_{min,k+L}^{chg,V}$, $I_{max,k+L}^{dis,V}$ can be formulated as Eq. (A15).

$$
\begin{cases}
I_{min,k+L}^{chg,V} = \dfrac{U_{OC}(z_k,Q_N) - \left(e^{-\frac{T_S}{\tau_1}}\right)^L U_{1,k} - \left(e^{-\frac{T_S}{\tau_2}}\right)^L U_{2,k} - U_{L,max}}{\dfrac{\eta L T_s}{Q_N}\dfrac{\partial U_{OC}}{\partial z}\bigg|_{Z=Z_k} + R_1\left(1-e^{-\frac{T_s}{\tau_1}}\right)\Sigma_{j=0}^{L-1}\left(e^{-\frac{T_s}{\tau_1}}\right)^{L-1-j} + R_2\left(1-e^{-\frac{T_s}{\tau_2}}\right)\Sigma_{j=0}^{L-1}\left(e^{-\frac{T_s}{\tau_2}}\right)^{L-1-j} + R_i} \\[6ex]
I_{max,k+L}^{dis,V} = \dfrac{U_{OC}(z_k,Q_N) - \left(e^{-\frac{T_S}{\tau_1}}\right)^L U_{1,k} - \left(e^{-\frac{T_S}{\tau_2}}\right)^L U_{2,k} - U_{L,min}}{\dfrac{\eta L T_s}{Q_N}\dfrac{\partial U_{OC}}{\partial z}\bigg|_{Z=Z_k} + R_1\left(1-e^{-\frac{T_s}{\tau_1}}\right)\Sigma_{j=0}^{L-1}\left(e^{-\frac{T_s}{\tau_1}}\right)^{L-1-j} + R_2\left(1-e^{-\frac{T_s}{\tau_2}}\right)\Sigma_{j=0}^{L-1}\left(e^{-\frac{T_s}{\tau_2}}\right)^{L-1-j} + R_i}
\end{cases} \quad (A15)
$$

Reference

[1] L. Fan, Y. Zhang, H. Dou, R. Zou, Design of an integrated energy management strategy for a plug-in hybrid electric bus, J. Power Sources 448 (2020) 227391. https://doi.org/10.1016/j.jpowsour.2019.227391.

[2] M. A. Soumeur, B. Gasbaoui, O. Abdelkhalek, J. Ghouili, T. Toumi, A. Chakar, Comparative study of energy management strategies for hybrid proton exchange membrane fuel cell four wheel drive electric vehicle, J. Power Sources 462 (2020) 228167. https://doi.org/10.1016/j.jpowsour.2020.228167.

[3] R. M. Prasad, A. Krishnamoorthy, Design validation and analysis of the drive range enhancement and battery bank deration in electric vehicle integrated with split power solar source, Energy, 172 (2019) 106-116. https://doi.org/10.1016/j.energy.2019.01.116.

[4] H. Fathabadi, Utilizing solar and wind energy in plug-in hybrid electric vehicles, Energy Convers. Manag. 156 (2018) 317-328. https://doi.org/10.1016/j.enconman.2017.11.015.

[5] Y. Zhang, X. Yuan, L. Duan, Y. Xu, F. Lan, Environmental temperature effects on the energy flow

of plug-in hybrid electric vehicles, J. Power Sources 506 (2021) 230231. https://doi.org/10.1016/j.jpowsour.2021.230231.

[6] Z. Xu, J. Wang, P. D. Lund, Y. Zhang, Estimation and prediction of state of health of electric vehicle batteries using discrete incremental capacity analysis based on real driving data, Energy 225 (2021) 120160. https://doi.org/10.1016/j.energy.2021.120160.

[7] R. Xiong, F. Sun, H. He, T. D. Nguyen, A data-driven adaptive state of charge and power capability joint estimator of lithium-ion polymer battery used in electric vehicles, Energy 63 (2013) 295-308. https://doi.org/10.1016/j.energy.2013.10.027.

[8] Y. Li, W. Wang, L. Cheng, X. Yang, F. Zuo, A safety performance estimation model of lithium-ion batteries for electric vehicles under dynamic compression, Energy 215 (2021) 119050. https://doi.org/10.1016/j.energy.2020.119050.

[9] S. Lee, J. Kim, J. Lee, B. H. Cho, State-of-charge and capacity estimation of lithium-ion battery using a new open-circuit voltage versus state-of-charge, J. Power Sources 185 (2) (2008) 1367-1373. https://doi.org/10.1016/j.jpowsour.2008.08.103.

[10] H. Li, Y. Wang, X. He, Q. Li, Z. Wang, Effects of structure parameters on thermal performance of ternary lithium ion battery under fast charging conditions, Energy Fuels 34 (7) (2020) 8891-8904.

[11] J. Meng, M. Ricco, G. Luo, M. Swierczynski, An Overview and Comparison of Online Implementable SOC Estimation Methods for lithium-Ion Battery, IEEE Trans. Ind. Appl. 54 (2) (2017) 1583-1591.

[12] J. Du, Z. Liu, Y. Wang, C. Wen, An adaptive sliding mode observer for lithium-ion battery

state of charge and state of health estimation in electric vehicles, Control Engineering Practice, 54 (2016) 81-90. https://doi.org/10.1016/j.conengprac.2016.05.014.

[13]   L. Zhao, Z. Liu, G. Ji, lithium-ion battery state of charge estimation with model parameters adaptation using H∞ extended Kalman filter, Control Engineering Practice 81 (2018) 114-128. https://doi.org/10.1016/j.conengprac.2018.09.010.

[14]   G. L. Plett, Sigma-point Kalman filtering for battery management systems of LiPB-based HEV battery packs: Part 2: Simultaneous state and parameter estimation, J. Power Sources 161 (2) (2006) 1369-1384. https://doi.org/10.1016/j.jpowsour.2006.06.004.

[15]   H. Ben Sassi, F. Errahimi, N. Es-Sbai, State of charge estimation by multi-innovation unscented Kalman filter for vehicular applications, J. Energy Storage 32 (2020) 101978. https://doi.org/10.1016/j.est.2020.101978.

[16]   S. Peng, X. Zhu, Y. Xing, H. Shi, X. Cai, M. Pecht, An adaptive state of charge estimation approach for lithium-ion series-connected battery system, J. Power Sources 392 (2018) 48-59, https://doi.org/10.1016/j.jpowsour.2018.04.101.

[17]   A. E. Mejdoubi, A. Oukaour, H. Chaoui, H. Gualous, Y. Slamani, State-of-charge and state-of-health lithium-Ion batteries' diagnosis according to surface temperature variation, IEEE Trans. Ind. Electron. 63 (4) (2015) 2391-2402.

[18]   G. L. Plett, High-performance battery-pack power estimation using a dynamic cell model, IEEE Trans. Veh. Technol. 53 (5) (2004) 1586-1593.

[19]   R. Xiong, H. He, F. Sun, X. Liu, Z. Liu, Model-based state of charge and peak power capability joint estimation of lithium-ion battery in plug-in hybrid electric vehicles, J. Power

Sources, 229 (2013) 159-169. https://doi.org/10.1016/j.jpowsour.2012.12.003.

[20]   J. Jiang, S. Liu, Z. Ma, L. Y. Wang, K. Wu, Butler-Volmer equation-based model and its implementation on state of power prediction of high-power lithium titanate batteries considering temperature effects, Energy 117 (2016) 58-72. https://doi.org/10.1016/j.energy.2016.10.087.

[21]   R. Xiong, H. Chen, C. Wang, F. Sun, Towards a smarter hybrid energy storage system based on battery and ultracapacitor - A critical review on topology and energy management, J. Cleaner Production 202 (2018) 1228-1240. https://doi.org/10.1016/j.jclepro.2018.08.134.

[22]   L. Jiang, Y. Li, Y. Huang, X. Qiao, Y. Wang, Y. Cao, Optimization of multi-stage constant current charging pattern based on Taguchi method for Li-Ion battery, Appl. Energy 259 (2019) 114148. https://doi.org/10.1016/j.apenergy.2019.114148.

[23]   M. Yin, C. Jeonghun, P. Daejin, Pulse-based fast battery IoT charger using dynamic frequency and duty control techniques based on multi-Sensing of polarization curve, Energies 9 (3) (2016) 209.

[24]   Y. Li, K. Li, Y. Xie, J. Liu, C. Fu, B. Liu, Optimized charging of lithium-ion battery for electric vehicles: Adaptive multistage constant current–constant voltage charging strategy, Renewable Energy, 146 (2020) 2688-2699. https://doi.org/10.1016/j.renene.2019.08.077.

[25]   J. Yang, B. Xia, W. Huang, Y. Fu, C. Mi, Online state-of-health estimation for lithium-ion batteries using constant-voltage charging current analysis, Appl. Energy 212 (2018) 1589-1600. https://doi.org/10.1016/j.apenergy.2018.01.010.

[26]   L. R. Chen, Design of duty-varied voltage pulse charger for improving Li-Ion battery-

charging response, IEEE Trans. Ind. Electron. 56 (2) (2009) 480-487.

[27]   S. Wang Y. Liu, A PSO-based fuzzy-controlled Searching for the optimal charge pattern of Li-Ion batteries, IEEE Trans. on Ind. Electron., 62 (5) (2015) 2983-2993.

[28]   Y. Liu, C. Hsieh, Y. Luo, Search for an optimal five-step charging pattern for Li-Ion batteries using consecutive orthogonal arrays, IEEE Trans. Energy Convers. 26 (2) (2011) 654-661.

[29]   M. Hu, Y. Li, S. Li, C. Fu, D. Qin, Z. Li, Lithium-ion battery modelling and parameter identification based on fractional theory, Energy 165 (2018) 153-163. https://doi.org/10.1016/j.energy.2018.09.101.

[30]   B. Amrouche, A. Guessoum, M. Belhamel, A simple behavioural model for solar module electric characteristics based on the first order system step response for MPPT study and comparison, Appl. Energy, 91 (1) (2012) 395-404. https://doi.org/10.1016/j.apenergy.2011.09.036.

[31]   J. Loukil, F. Masmoudi, N. Derbel, A real-time estimator for model parameters and state of charge of lead acid batteries in photovoltaic applications, J. Energy Storage 34 (2021) 102184. https://doi.org/10.1016/j.est.2020.102184.

[32]   Y. Y. Choi, S. Kim, S. Kim, J.-I. Choi, Multiple parameter identification using genetic algorithm in vanadium redox flow batteries, J. Power Sources 450 (2020) 227684. https://doi.org/10.1016/j.jpowsour.2019.227684.

[33]   J. Zhu, M. Knapp, D. Sorensen, M. Heere, M. Darma, M. Muller, L. Mereacre, Investigation of capacity fade for 18650-type lithium-ion batteries cycled in different state of charge (SoC)

ranges, J. Power Sources 489 (2021) 229422. https://doi.org/10.1016/j.jpowsour.2020.229422.

[34]   Z. Zhang, L. Jiang, L. Zhang, C. Huang, State-of-charge estimation of lithium-ion battery pack by using an adaptive extended Kalman filter for electric vehicles, J. of Energy Storage 37(2021) 102457. https://doi.org/10.1016/j.est.2021.102457.

[35] J. Yang, B.Xia, W. Huang, Y. Fu, C. Mi, Online state-of-health estimation for lithium-ion batteries using constant-voltage charging current analysis, Appl. Energy 212 (2018) 1589-1600. https://doi.org/10.1016/j.apenergy.2018.01.010.